

## CRACK GROWTH AND FAULTING IN CYLINDRICAL SPECIMENS OF CHELMSFORD GRANITE

S. PENG\* and A. M. JOHNSON

Departments of Mineral Engineering and Geology, Stanford  
University, Stanford, California

(Received 18 November 1970)

**Abstract**—This study focuses on processes of fracture propagation and faulting in specimens of Chelmsford granite subjected to various end-boundary conditions and confining pressures. Chelmsford granite is a brittle material and contains numerous small defects which are preferentially oriented along three mutually perpendicular planes. The defects significantly affect the physical properties of the granite and the way the granite fails.

Theoretical solutions for stresses within cylindrical elastic bodies indicate that stresses within a test specimen are markedly nonuniform. The stresses are not simply axial and equal to the axial load divided by the cross-sectional area of the specimen, as is assumed by many rock mechanacists.

Regardless of end-boundary conditions of specimens, cracks in Chelmsford granite propagate parallel to the direction of axial loading. Cracks in a specimen of granite, with thin neoprene inserts or teflon inserts placed between its ends and the loading platens, grow most intensely near the longitudinal axis, at the ends of the specimen. A theoretical solution for stresses in specimens subjected to these end conditions indicates that compressive axial stresses and tensile radial stresses are maximum in those places. Thus, a combination of Griffith's theory of crack propagation and the theoretical solution for stresses seems to account for the observed crack pattern.

*Uniform loading* was achieved for Chelmsford granite by inserting specially made steel discs between a specimen and the platens of the loading machine. Cracks in specimens subjected to uniform loading propagate relatively uniformly throughout the specimens, as predicted by theory.

Specimens subjected to end-boundary conditions of uniform loading or of teflon inserts or of neoprene inserts, fail by longitudinal splitting, parallel to the direction of axial loading, and then by buckling of the split slabs.

Specimens that were placed in *direct contact* with the relatively rigid platens of the loading machine also are stressed highly nonuniformly. The areas of most intense crack growth are two bands, extending from the corners of a specimen to a distance of about one-quarter of the specimen height from the specimen ends, as predicted theoretically.

The specimens of granite subjected to direct contact end conditions or to triaxial loading, regardless of end condition, fail by *faulting*. The type of faulting depends on frictional properties of the platens. The fault surfaces consist of small steps, arranged as in a staircase. The surfaces of the steps are roughly perpendicular to the loading axis of a specimen and the vertical risers are surfaces of cracks that have propagated axially. Thus, immediately before faulting occurs, a specimen appears as though it consists of closely fitting, tiny beams, bounded by axial cracks.

We have developed a theory of faulting of specimens of Chelmsford granite, based on beam-buckling theory and frictional contact among beams. The theory seems to describe relations between average ultimate compressive strengths and confining pressures, ranging from zero to 10,000 psi, for samples of Chelmsford granite. Neither the Coulomb criterion nor the modified Griffith criterion fit the experimental data.

### 1. INTRODUCTION

FRACTURE of rock has been a subject of intensive study by rock mechanacists, structural geologists and structural petrologists for many years. Rock mechanacists in mining and civil engineering have been concerned largely with the compressive strength of rock in

\* Present address: U.S. Bureau of Mines, Minneapolis, Minn.

their attempts to design rock structures, such as slopes in open-pit mines, underground openings of various types and foundations of dams [1-6]. Thus, the elastic properties and the ultimate compressive strengths of rock in the area of a future opening usually are considered to be crucial factors in the design of a deep underground opening. Many questions immediately arise about strength as a factor of design, including those about what rock strength is, what values of strength should be used for design purposes, and, more fundamentally, is strength actually an important property for a given design problem.

Structural geologists, on the other hand, primarily have been concerned with the meanings of fracture patterns which they believe they can recognize in the field, at scales ranging from a few millimeters in rock thin-sections, to many kilometers, both on the continents and in oceanic basins. Writings of ANDERSON [7] and HUBBERT [8] are responsible for the recognition, by geologists in general, of the similarities between orientations of failure planes in soils, as predicted by Coulomb's criterion, and orientations of faults in nature. Griggs and other structural petrologists have emphasized the similarities between orientations of faults in specimens of rock on the one hand and orientations predicted by Coulomb's criterion and orientations of natural faults and joints on the other [9-11].

Several practical and theoretical problems are introduced by the use of laboratory test results to predict failure of rock around underground openings and by the use of laboratory tests or failure criteria to predict orientations of natural faults. One problem is confusion about the meaning of failure criterion. Coulomb's criterion apparently was introduced to describe deformation of granular solids which behave much as plastic substances, for which it seems to work quite well. The criterion, therefore, describes the critical state of stress near a point within a certain type of plastic substance. It is not simply an empirical rule because it has been derived theoretically and related to contact friction and interlocking of spherical particles [12]. Application of Coulomb's criterion to faulting of brittle rock by many geologists [7-9] however, is open to serious question. The fundamental problem with the application of Coulomb's criterion to brittle fracture is that there is no theoretical basis for such an application, so that it has no meaning. Even if we assumed, for some reason, that Coulomb's criterion applied to the formation of a shear crack in a small area of a specimen, we still could not predict the orientation of the final fracture. Once the crack has opened, as shown by INGLIS [13], the state of stress in the vicinity of the crack is changed markedly. Thus, Coulomb's criterion cannot predict the direction of *propagation* of a crack and it cannot predict the orientation of a fracture in brittle materials.

Perhaps the problem is with terminology and that there was no intent by early investigators to correlate the modern concept of a brittle-elastic material with the behaviors of most rock. Thus, the close correlation, recognized by ANDERSON [7] and HUBBERT [8] between orientations of faults in nature and faults in rock specimens on the one hand and orientations of shear planes predicted by Coulomb's criterion on the other might indicate *plastic* behavior of the rocks. It remains to be demonstrated whether deformation of rock, on the scale of geologic faults, involves the types of processes of deformation acting within granular materials, for which Coulomb's criterion is a possible theoretical model.

The application of Griffith's criterion to brittle rock has a theoretical foundation. GRIFFITH [14,15] and INGLIS [13] recognized that most brittle materials, such as glass, fail at applied stresses much lower than the theoretical strengths of the materials. Griffith postulated that materials contain randomly oriented cracks which significantly alter stress fields within the materials. The stresses at tips of slender cracks within a material increase several orders of magnitude above the applied stresses and where local stresses exceed the theoretical

strength of the material, according to Griffith, the cracks propagate and cause fracture. Thus, Griffith's theory also is based on theoretical analysis of a mechanism of deformation [16].

Even Griffith's criterion is beset with problems, however. One is that it, also, does not predict the orientation of fracture propagation for most states of stress associated with faulting. BRACE and BOMBOLAKIS [17] and HOEK [18] have shown that when a plate containing an isolated, inclined crack is subjected to biaxial compression, the maximum tensile stress along the crack boundary does not occur at the crack tip. Instead, it may be on the crack boundary, near the tip. Therefore, theory predicts and idealized experiments demonstrate that crack growth will occur near, but not at, the ends of the original crack so that the direction of crack propagation is not in the plane of the original crack. BRACE and BOMBOLAKIS [17] and HOEK and BIENIAWSKI [19] showed that inclined cracks tend to propagate out of their planes, and to become parallel to the direction of maximum compression of brittle-elastic plates containing the cracks.

Neither Griffith's nor Coulomb's theories, therefore, can predict orientations of faults in brittle-elastic materials in the field or in the laboratory [20].

Another problem with most applications of fracture theories is that stresses within the bodies considered usually are assumed to be uniform whereas they normally are not. Thus, many structural petrologists assume that the axial stress at any point within a cylindrical sample loaded in a testing machine is equal to the axial force divided by the cross-sectional area of the sample. It has been recognized, at least since 1902, however, that stresses within cylindrical specimens are nonuniform and depend upon end-boundary conditions of the specimens [21-27]. Without knowing the stress distribution within a specimen, therefore, theoretically it is not even possible to predict orientations of cracks that will initiate within a brittle-elastic material loaded in a testing machine.

Our study focuses on the processes of fracture propagation and faulting within specimens of a granite from North Chelmsford, Mass. The questions we are attempting to answer are: What does compressive strength of Chelmsford granite really mean? How do large, megascopic fractures develop in cylindrical specimens of Chelmsford granite?

We hope that, if we can understand how fractures develop in a type of rock with which we are familiar, and under conditions we can control and describe quite completely, we thereby can learn something about the way fractures develop in all similar rock types subjected to similar conditions. Thus, we are attempting to study processes of fracture of Chelmsford granite. The knowledge that we gain about these processes should be applicable to many rock types.

The method of our research is a combination of theoretical and laboratory investigations. The laboratory work involves the identification of microdefects in Chelmsford granite, the investigation of end-boundary conditions likely to occur in laboratory testing, and the determination of strength and modes of fracture of Chelmsford granite under various end-boundary conditions.

The theoretical investigation [25, 26] is an analysis of stress and strain distributions in cylindrical specimens, taking into account the boundary conditions likely to occur in the laboratory. Different boundary conditions produce different stress and strain distributions in cylindrical specimens. Theoretical stress distributions will be used here to interpret the different ultimate strengths and the modes of fracture of Chelmsford granite under the various boundary conditions.

The broader questions about meanings of patterns of geologic faults and joints and the usefulness of laboratory testing for engineering design are not answered here. However, the

types of problems discussed here must be solved before we can answer meaningfully the broader questions.

## 2. CHARACTERISTICS OF CHELMSFORD GRANITE

Almost any material can fracture, including materials ranging from soft clay slurries to brittle glasses. However, the mechanisms of fracture probably are different in different materials. In order to simplify our study of fracture, we wanted to be able to apply the relatively vast background of knowledge already accumulated in the theories of linear fracture mechanics [28]. This group of theories applies to brittle-elastic materials, so that we selected an experimental material whose properties closely approximate brittle-elastic behavior. Among rocks, granitic rocks and quartzite are most nearly brittle [29, 30]. Another factor that governed our selection of an experimental material was that of rock fabric and texture. We wanted a rock that is quite thoroughly known, both compositionally and texturally. Richard H. Jahns, Frederick C. Kruger, and the junior author, of Stanford University, have been studying various aspects of the Chelmsford granite in the H. E. Fletcher Quarry at North Chelmsford, Mass., so that this granite seemed to be a logical choice for the experimental studies.

### 2.1 Composition and texture

Chelmsford granite is quarried by H. E. Fletcher Co. of North Chelmsford, Mass. It is light bluish-gray in color.\* The primary minerals are quartz, plagioclase and potassium feldspar, muscovite and biotite. Epidote, chlorite and calcite are secondary. Deuteric reactants are present, such as biotite to chlorite, muscovite to chlorite and biotite to epidote. Some mica flakes and plagioclase tablets are bent. Quartz characteristically occurs as fine-grained aggregates. Long streaks of fine-grained muscovite and epidote occur along grain boundaries.

Chelmsford granite contains about 35 per cent microcline and 25 per cent plagioclase by volume, with an average grain size of 0·109 in., and contains 31 per cent quartz by volume, with grain sizes ranging from 0·008 to 0·050 in. and averaging 0·024 in. Muscovite content is about 5 per cent and biotite content is 1 per cent by volume.

Relative percentages of microcline, plagioclase and quartz are used by BATEMAN [31] to classify granite rocks. Based on his classification, Chelmsford granite is, mineralogically, a quartz monzonite. According to JAHNS [32] it is granite in terms of chemical composition. In

TABLE 1. AVERAGE CRYSTAL SIZES IN CHELMSFORD GRANITE\*

Direction	Quartz	Mica	Feldspar
Rift plane	33·7 × 21·0	35·4 × 14·9	166·7 × 45·4
Hardway plane	22·4 × 13·3	22·8 × 8·2	154·0 × 36·5
Grain plane	34·5 × 19·6	39·6 × 11·1	158·2 × 38·9
Average	30·9 × 18·9	32·6 × 11·4	160·0 × 40·3

\* Measured in thousandths of an inch.

\* The following description is by Arthur Snode and James Blencoe, graduate students, Stanford University.

the commercial trade, the rock is called granite. The terms granite and Chelmsford granite will be used in following discussions.

Table 1 shows average grain sizes of the three principal constituents; feldspar (both plagioclase and potassium feldspar), quartz and mica (mostly muscovite). The numbers given are averages of the largest and shortest dimensions of each constituent.

It is well known [33-35] that most granites possess three sets of orthogonal cleavages, or directions of easy splitting. These usually are called 'rift', 'grain' and 'hardway', in order of ease of splitting. The rift of Chelmsford granite is horizontal, the grain is vertical, and the hardway is perpendicular to both rift and grain, and strikes about N45°W.

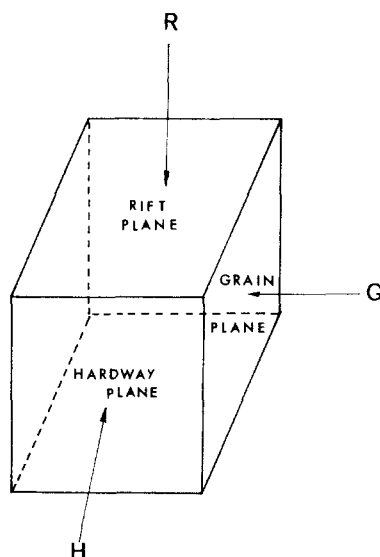


FIG. 1. Directional symbols used to identify quarry directions in samples of Chelmsford granite. *Rift* is horizontal in Fletcher granite quarry and is direction of easiest splitting. *Grain* is vertical and is direction of next easiest splitting. *Hardway* is vertical and is direction of next easiest splitting. The symbols, *R*, *G* and *H* refer to *normals* to planes of rift, grain and hardway, respectively.

Samples of Chelmsford granite were donated by H. E. Fletcher Co., Mass. They were in blocks with dimensions of  $6 \times 8 \times 10$  in. (Fig. 1) and with faces parallel to the rift, grain and hardway planes. Figure 1 shows the directional convention used in the following pages. The letters *R*, *G*, and *H* refer to normals to rift, grain and hardway planes, respectively. Specimens were cored parallel to the *R*-, *G*- and *H*-directions. Thus, the symbols *R*, *G* and *H* specify orientations of specimens discussed in the following pages. For example, an *R*-specimen is a core, the long axis of which is perpendicular to the rift plane.

## 2.2 Fabric analysis

Many investigators of fracture mechanics have adopted Griffith's theory, which postulates that small Griffith cracks enlarge into fractures [18, 29, 30]. The question is, then, what are Griffith cracks? BRACE [36] suggested that grain boundaries correspond to Griffith cracks and that their maximum lengths are on the order of maximum diameters of grains. HOEK [18] assumed that Griffith cracks are *en echelon* cracks along grain boundaries. Nobody,

however, has made a careful study of initial cracks or has made a serious attempt to relate these cracks to the final fracture. In addition, grain-boundary cracks certainly are not the only kinds of defects that can be classed as Griffith cracks.

Universal Stage techniques were used in order to determine orientations of open cracks and orientations of minerals in samples of Chelmsford granite. Thin sections were cut parallel to rift, grain and hardway planes in each granite block. Quartz optic axes and three types of planar features were measured: microcracks, feldspar twin planes and (001) cleavage of mica flakes. Measurements of planar features and optic axes were made for all grains in thin sections with areas of 10 cm<sup>2</sup>. The sections were traversed by turning the mechanical stage so that the grid points covered entirely new areas. The fabric elements were plotted on individual stereonets.

All open visible microcracks within quartz and feldspar grains were measured; microcracks filled with mica were ignored. Microcracks are defined operationally in this study as distinct planes which appear as sharp, thin lines when rotated with the horizontal Universal Stage axis oriented parallel to their traces and which, under high magnification, appear as open fissures. Frequently, a single open crack changes orientation abruptly in several places along its length (Fig. 2). In such cases the orientation of each segment was recorded separately. The orientations of a curviplanar crack on the other hand was represented by an average orientation for the entire microcrack.

Three types of microcracks were measured: intergranular and transgranular microcracks in quartz grains and transgranular microcracks in feldspar grains. *Intergranular microcracks* are grain-boundary cracks. *Transgranular microcracks* are cracks that cut across mineral grains. Average lengths of intergranular microcracks are the same as the average diameters of quartz grains, whereas average lengths of transgranular microcracks are greater than the diameters of the grains and the cracks extend into neighboring quartz grains (see Table 2). Transgranular microcracks in feldspar grains are usually perpendicular to twin planes. They are much shorter than the grains and they appear in groups parallel to each other, that is, they are *en echelon*.

Transgranular microcracks in quartz and feldspar show strong preferred orientations parallel to the rift plane [see Figs 3(a) and 3(b)]. Cracks in feldspar also show a secondary preferred orientation parallel to the hardway plane. Figures 3(a) and 3(b) were produced by studying thin sections oriented parallel to rift, grain and hardway directions and then by combining all the data on equal-area stereonets. Figure 3(c) shows the distributions of all microcracks; it was constructed by combining the data shown in Figs 3(a) and 3(b). The total number of microcracks measured was 672 in the three thin sections. The composite stereonet, Fig. 3(c), shows a strong preferred orientation of microcracks parallel to the rift plane [ $R$  in Fig. 3(c)], a secondary preferred orientation of microcracks lying between 7 and 12° from the grain plane and a weak preferred orientation of microcracks subparallel to the hardway plane. Presumably, this alignment of microcracks accounts for the greatest ease of splitting along the rift plane.

Chelmsford granite contains about 6 per cent of mica, and mica possesses a markedly weak plane of cleavage which might act as a Griffith crack. Figure 4(a) is a composite stereonet diagram of mica cleavage orientations, produced by studying thin sections oriented parallel to rift, grain and hardway directions and by rotating the data into the plane of Fig. 4(a). Cleavages of 323 mica flakes were measured. There is a strong preferred orientation of mica cleavages parallel to the grain plane. The preferred orientation of mica cleavages might partly explain the ease of splitting of Chelmsford granite along the grain plane.



FIG. 2. Types of microcracks identified in Chelmsford granite; (A) *intergranular* or grain-boundary crack between quartz grains; (B) *transgranular* crack within quartz; (C) *transgranular* crack within feldspar.

TABLE 2. MEASUREMENTS OF MICROCRACKS IN CHELMSFORD GRANITE\*

Direction	inter—†			Quartz			trans—†			Feldspar inter—†		
	Number	Av. length	Percentage	Number	Av. length	Percentage	Number	Av. length	Percentage	Number	Av. length	Percentage
Rift plane	134	28·0	76·6	12	15·3	3·7	48	20·1	19·7			
Hardway plane	192	23·5	44·1	84	31·4	25·8	117	26·7	30·1			
Grain plane	126	23·9	37·7	62	34·0	26·2	184	25·6	35·9			
Total	452	25·0	48·9‡	158	31·2	21·4‡	349	19·7	29·7			
						16·5§						

\* All numbers in the table are in thousandths of an inch.

† Inter- and trans-granular cracks.

‡ Total percentage by length.

§ Total percentage by number.

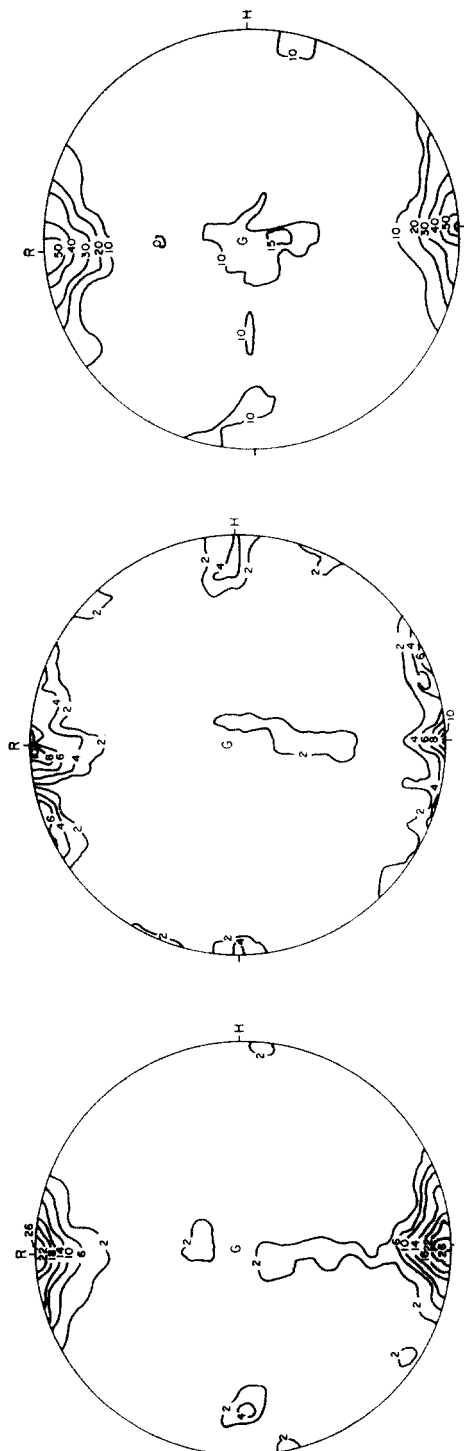


FIG. 3. Stereonet contour diagrams of frequency of poles to microcracks in Chelmsford granite. Equal-area net was used as base.  
 (a) Transgranular microcracks in quartz. (b) Transgranular microcracks in feldspar. (c) Composite of all transgranular and intergranular microcracks in quartz and feldspar.



FIG. 4. Stereonet contour diagrams of frequency of poles to (a) nica cleavage, (b) twin planes of feldspar grains and (c) optic axes of quartz grains.

Orientations of feldspar twin planes relative to rift, grain and hardway directions are shown in Fig. 4(b), as determined by measuring 221 grains. Although there are several directions of preferred orientation, they all are minor. Similarly, Fig. 4(c) shows that there is no preferred orientation of quartz optic axes in the sample studied.

JAHNS [32] has mapped the H. E. Fletcher Quarry and studied the granite in thin sections. He found that most cracks and fluid inclusions in quartz grains are parallel to the rift plane, and that some of them are parallel to both the grain and the hardway planes. He also found that mica cleavage is not parallel to the grain plane but that, instead, it is inclined about 5° to the grain plane. Therefore, according to Jahns, the ease of splitting along the grain cannot be attributed entirely to preferred orientation of mica cleavages. The difference in orientation between the grain plane and the preferred orientation of mica cleavage is so small, however, that when cracks propagate parallel to the grain plane, they tend to step to follow the direction of mica cleavage. Therefore, he stated, a fracture on the grain plane feels rough when rubbed in one direction, but feels smooth when rubbed in the opposite direction.

These fabric analyses indicate strong preferred orientation of microcracks parallel to the rift plane and weak preferred orientation of microcracks in the direction of the grain plane [Fig. 3(c)]. There are strong preferred orientations of mica cleavages parallel to the grain plane and weak preferred orientations parallel to the hardway plane [Fig. (4a)]. Perhaps the rift plane is the direction of easiest splitting because of the strong preferred orientation of microcracks. The weak preferred orientation of microcracks and the strong preferred orientation of mica cleavages along directions parallel to the grain plane presumably account for the ease of splitting along the grain plane. A weak preferred orientation of mica cleavages parallel to the hardway plane probably explains why it is the most difficult direction of splitting among the rift, grain and hardway planes.

If these preferred orientations of microcracks can be used to explain the ease of splitting along the rift, grain and hardway planes, we would expect several other directions of ease of splitting in Chelmsford granite, because Figs 3(c) and 4(a) show that there are several weak preferred orientations of microcracks and of mica cleavages other than those parallel to rift, grain and hardway planes. This effect will be explored in Section 2.4 when we describe measurements of tensile strength.

### 2.3 *Young's moduli and Poisson's ratios*

The most common method of studying mechanical properties of rocks is by axial compression of circular cylinders, the lengths of which are twice the diameters. Normally, forces are applied to the ends of a cylinder and the axial and lateral strains are measured with strain gages attached to the cylindrical surface. In order to eliminate bending strain, readings of two gages, mounted on the diametrically opposite sides of the cylinder, are averaged. They are attached at midheight on the specimen so that end effects are minimized. The hope usually is that the gages are measuring the average axial and transverse strains within as well as on the surface of the sample. This hope generally is not realized, but we will postpone a detailed discussion of actual strains to following pages.

Similarly, stress within a cylindrical sample usually is considered to be equal to the force, applied to each end of the sample by a loading machine, divided by the area of one end of the sample. This also, is a gross over-simplification, as has been demonstrated by PENG [25, 26].

Here, we wish simply to illustrate the general 'stress-strain' behavior of Chelmsford granite by showing relations between average axial stresses and strains measured on the surfaces of cylindrical samples.

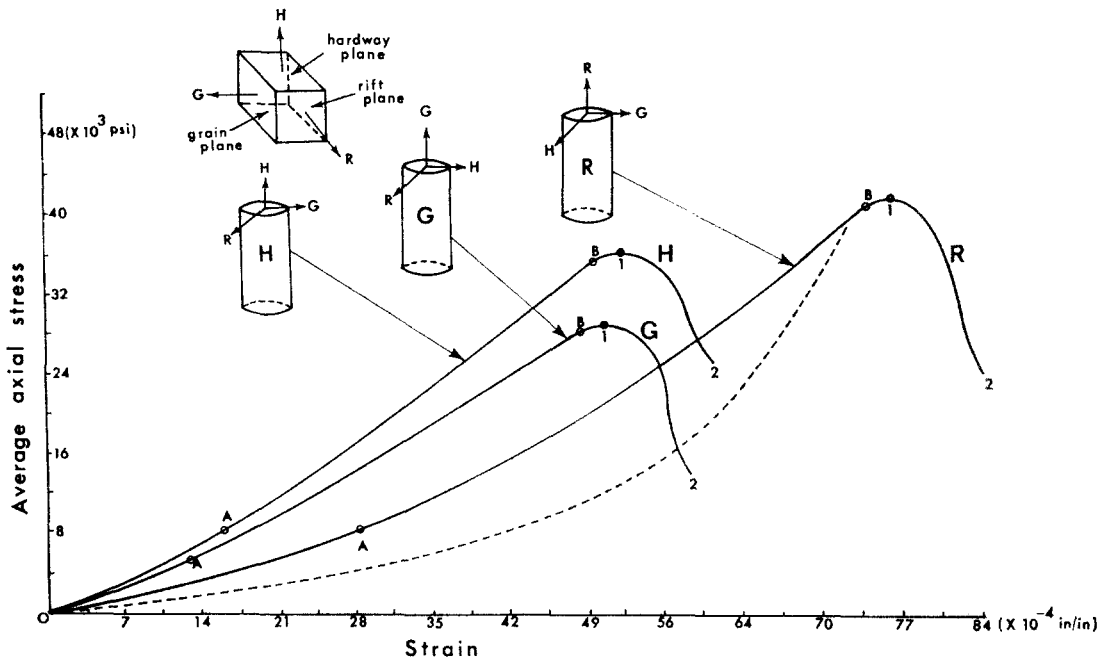


FIG. 5. Stress-strain relations for samples of Chelmsford granite loaded normal to rift (*R*), grain (*G*) and hardway (*H*) quarry directions. Solid lines are loading curves. Dashed line is unloading curve for *R* specimen loaded to near point *B* on stress-strain curve.

Figure 5 shows average-stress-average-strain curves for samples of which the axes were normal to rift, grain or hardway, as is indicated in the figure. The part of the curve from the origin to point 1 is the general stress-strain curve obtained without a stiffening element. The extended curves, to point 2, were obtained with a stiffening element. The load-bearing capacity of the specimen reduces when the specimen is loaded to point 1. At that time, if the machine system is not stiff enough, the elastic energy stored in the machine quickly releases, the machine rebounds, and the specimen is destroyed. When this happens, the behavior of the fractured specimen cannot be studied. Therefore, it is necessary to stiffen the machine or the specimen in order to study the complete strain-stress curve of the material. Since it is much easier and much less costly to stiffen the specimen than the machine, the specimen was stiffened by means of a stiffening element, loaded in parallel with the specimen (see PENG [25], Appendix III, for details of the design).

If the applied stress is released before the peak is reached, the strain disappears completely, so that, in this respect, Chelmsford granite is perfectly elastic. However, the unloading curves are different from the loading curves. Figure 5 indicates that the initial part, part *O-A*, of the stress-strain curve for specimens with ends parallel to the rift plane, curve *R*, is quite non-linear. It becomes linear with an average applied stress of 11,700 psi, or  $8.1 \times 10^7$  N/m<sup>2</sup>. A less striking nonlinearity is shown in curves *G* and *H*, representing relations for grain and hardway specimens, respectively. Perhaps the initial nonlinear behavior can be attributed to the existence of microcracks. Thus, perhaps the granite behaves as a linearly elastic material only after many of the preexisting microcracks are closed [17, 18]. This tentative conclusion correlates with the observation that most of the cracks are aligned parallel to the rift plane.

TABLE 3. POISSON'S RATIOS OF CHELMSFORD GRANITE

$$\begin{array}{lll} \nu_{RH} = 0.13^* & \nu_{GR} = 0.10 & \nu_{HG} = 0.11 \\ \nu_{RG} = 0.12 & \nu_{GH} = 0.11 & \nu_{GR} = 0.10 \end{array}$$

\* The first subscript of  $\nu$  is the direction of axial loading of the specimen and second subscript is the direction of measurement of Poisson expansion, that is, the direction of measurement of the strain gage.

Table 3 shows values of Poisson's ratio for Chelmsford granite as a function of the three directions. The values of Poisson's ratio were measured for a confining pressure of 8000 psi axial load. Poisson's ratio is essentially independent of orientation, maintaining a value of about 0.11.

Figure 6 shows average tangent Young's moduli at various applied stresses. Young's modulus normal to the rift is lowest, presumably due to the alignment of microcracks parallel to the rift. Young's modulus normal to the hardway plane is the highest. The tangent Young's modulus for the *R*-specimen increases linearly at the rate of 200 psi/psi and becomes constant at  $4.75 \times 10^6$  psi ( $3.28 \times 10^{10}$  N/m<sup>2</sup>) when the applied stress reaches

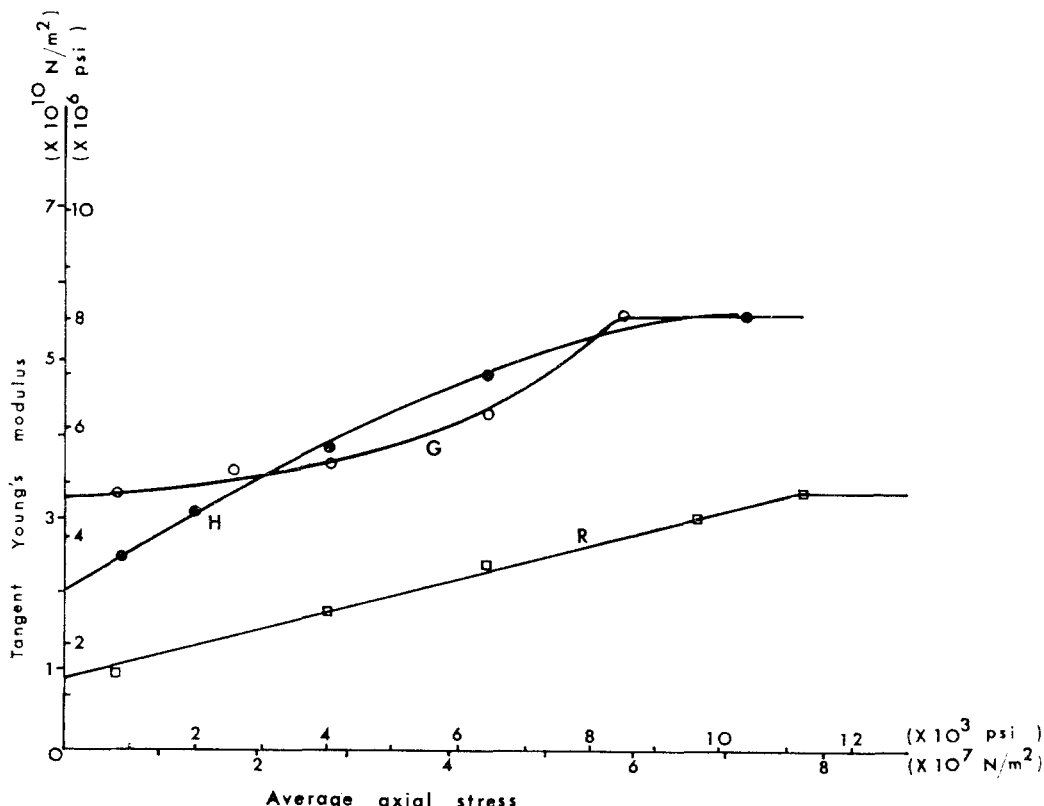


FIG. 6. Relations between tangent Young's modulus of Chelmsford granite and average axial stress for samples loaded normal to rift (*R*), grain (*G*) and hardway (*H*).

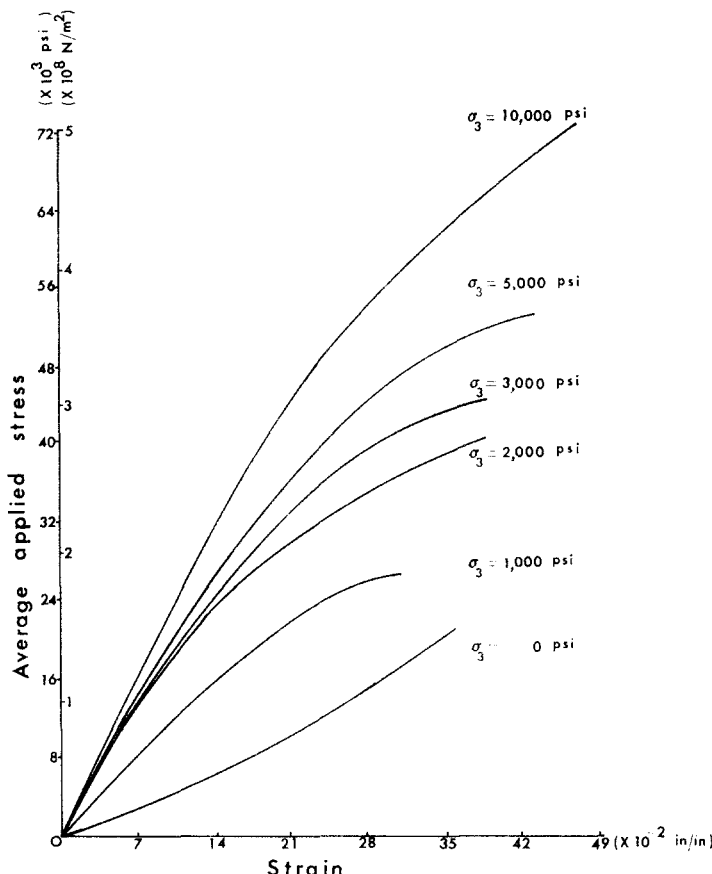


FIG. 7. Stress-strain relations for *G*-specimens of Chelmsford granite loaded to failure and subjected to various confining pressures.

11,690 psi ( $8.05 \times 10^7$  N/m $^2$ ). For *G*- and *H*-specimens, the increase of tangent Young's modulus during the initial part of loading is nonlinear, but becomes constant at about  $8.11 \times 10^6$  psi ( $5.6 \times 10^{10}$  N/m $^2$ ) at an applied stress of 9000 psi ( $6.2 \times 10^7$  N/m $^2$ ).

Figure 7 shows stress-strain curves for *G* samples subjected to various confining pressure. The strength and total strain at failure increase as confining pressure increases. Further, the initial nonlinear parts of the stress-strain curves shown in Fig. 5 disappear when the sample is subjected to confining pressure. Perhaps the confining pressures were sufficient to close many of the preexisting microcracks, thereby strengthening and stiffening the rock.

#### 2.4 Ultimate strengths

**Tensile strength.** The fabric analyses showed that microcracks and mica cleavages in Chelmsford granite have strong preferred orientations. Accordingly, we would expect tensile strengths of the granite to be different in different directions. Indeed they are, as can be shown by performing the standard Brazilian tensile test.

The Brazilian test is an indirect method for determining tensile strength of rock [4, 16]. The basic concept of the test is simple: When a circular disc is loaded by diametrically

opposed point loads, a uniform tensile stress develops across the diametral plane. One minor problem is that the elastic solution for stresses in the disc include a stress singularity at the points of loading. Also, experiments show that a wedge fracture forms at those loading points. In order to eliminate effects of wedging on measurements of tensile strength, the load was applied over an arc of  $15^\circ$  in our experiments. The radius of curvature of the loading platens is the same as the radius of the disc specimens. The change of stress distribution in the specimen, due to a load along an arc should be negligible, according to the Saint Venant principle.

Tensile strengths were measured for diametral directions at  $10^\circ$  intervals, from zero to  $90^\circ$ , from the rift to the grain directions or from the rift to the hardway directions. In order to check reproducibility, the tests were duplicated. Figure 8(a) shows the tensile strength variation for discs cut parallel to the hardway plane. It shows that tensile strength is quite variable, but definitely lowest along the rift plane, somewhat higher along the grain plane, and generally higher in other directions. The tensile strength is about  $850$  psi ( $5.86 \times 10^6$  N/m $^2$ ) parallel to the rift and is  $975$  psi ( $6.83 \times 10^6$  N/m $^2$ ) parallel to the grain, and ranges from about  $925$  psi ( $6.38 \times 10^6$  N/m $^2$ ) to  $1200$  psi ( $8.28 \times 10^6$  N/m $^2$ ) in other directions. There are two valleys in Fig. 8(a), corresponding with angles of  $35$  and  $70^\circ$  to the rift plane. Low tensile strength in these directions presumably can be attributed to secondary preferred orientations of microcracks [Fig. 3(c)] and mica cleavages [Fig. 4(a)] at

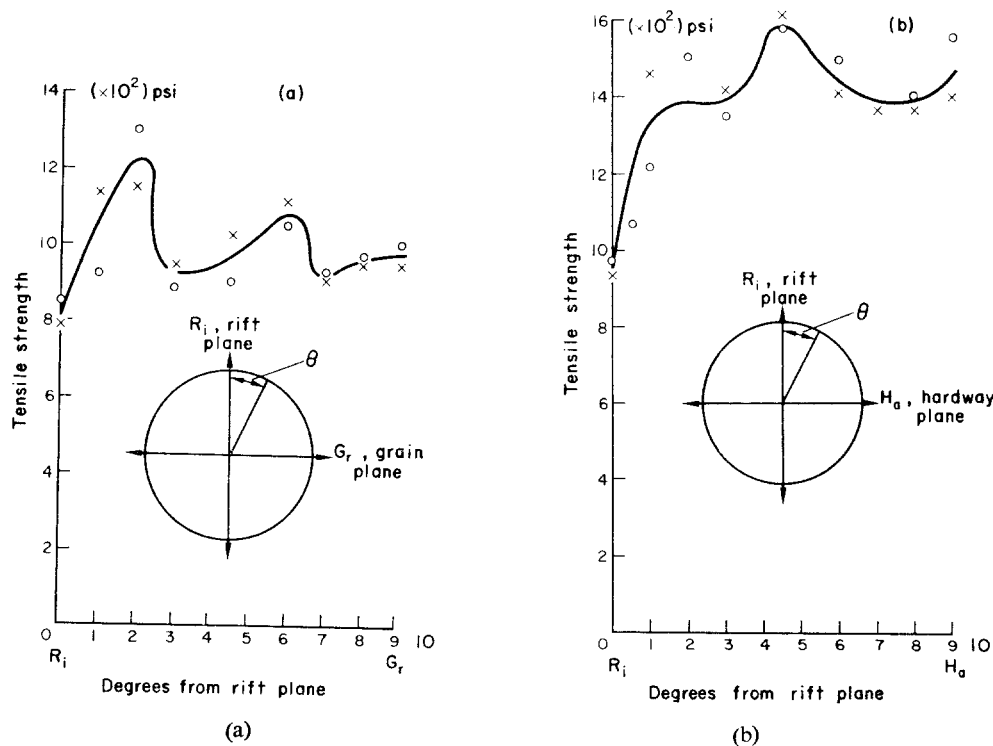


FIG. 8. Brazilian tensile strength of discs of Chelmsford granite as a function of direction of diametral loading relative to quarry directions.

(a) Discs with flat surfaces parallel to hardway plane. (b) Discs with surfaces parallel to grain plane.

these two orientations, while the two hills are due to lack of preferred orientation of micro-defects. Thus, the results correlate with the orientations of defects.

Tests with discs with rotational axes parallel to the normal of the grain plane [Fig. 8(b)] show similar strength variations. Strength increases sharply as the loading direction is inclined 10° and then 40° to the rift plane, reaching a strength of about 1600 psi ( $1 \cdot 10 \times 10^7$  N/m<sup>2</sup>) at an inclination of 40°. It decreases a little as the loading direction approaches the direction of the hardway plane, along which the strength is about 1450 psi ( $10^7$  N/m<sup>2</sup>). The tensile strength reaches a plateau between  $\theta = 15^\circ$  and  $30^\circ$ , presumably due to secondary preferred orientations of microcracks [Fig. 3(c)] and mica cleavage [Fig. 4(a)]. The increase in tensile strength between  $\theta = 36^\circ$  and  $65^\circ$  is due to the lack of preferred orientation of microdefects along those directions. Other secondary preferred orientations of micro-cracks and mica cleavages cause the decrease in tensile strength at an orientation of  $\theta = 75^\circ$ .

*Compressive strength.* As will be shown in Section 5, the ultimate compressive strength of Chelmsford granite varies from specimen to specimen. Also, concentrations of micro-cracks and end-boundary conditions markedly affect compressive strength of the granite. Therefore, we simply remark at this point that the uniaxial compressive strength of the granite ranges from 15,000 psi ( $1 \cdot 06 \times 10^8$  N/m<sup>2</sup>) to 29,000 psi ( $2 \times 10^8$  N/m<sup>2</sup>), and that average ultimate compressive strength is highest for *R*-specimens and lowest for *G*-specimens.

## 2.5 Fracture toughness

A physical property which is well known in Materials Science [28] but essentially unknown in rock mechanics is *fracture toughness*. The concept of fracture toughness is closely related to the theory of linear fracture mechanics which was introduced by GRIFFITH [14, 15] and supplemented by WESTERGAARD [37] and SNEDDON [38] and was further developed by IRWIN [39]. According to Griffith, crack propagation in a material creates new surfaces and associated surface energy, reducing the elastic strain energy stored within the material. As a crack lengthens, the rate of release of strain energy with a further increase in crack length reaches a critical value, at which crack propagation becomes unstable [16, 28]. Fracture toughness is related to the critical rate of energy release [28].

According to SNEDDON [38] and IRWIN [39], the stress field around a sharp elliptic crack is:

$$\sigma_{ij} = \frac{\sigma\sqrt{a}}{\sqrt{r}} f(\theta) = \frac{K}{\sqrt{r}} f(\theta)$$

where  $\sigma_{ij}$  is the stress tensor,  $\sigma$  is the applied stress,  $a$  is half the crack length,  $r$  is the radial distance from the sharp tip of the crack,  $\theta$  is the angle between the radial direction and the horizontal axis and  $K$  is the stress-intensity factor. The stress-intensity factor is the only variable parameter in the equation so that identical stress fields give identical values of  $K$ . Now, the critical stress system under which fracture occurs is characterized by a certain stress-intensity factor which is called *fracture toughness*,  $T_c$ . For many materials, fracture toughness is a material constant as is Young's modulus [28]. Thus, fracture toughness describes the conditions of failure of a Griffith substance without the necessity of considering details of processes of energy dissipation. It is a function of both the applied stress and the crack length, so that it can be obtained by testing specimens containing cracks of known orientations and sizes.

A satisfactory test of fracture toughness is one in which the specimen dimensions and the loading conditions are such that the value of the stresses at the crack tip and the crack length are known at any stage of the test. Experiments [40] show that the area that becomes plastic

around the crack tip must be small so that it is negligible as compared with the dimensions of the specimen or of the crack. The minimum necessary dimensions of a specimen of a given type increase rapidly as the yield strength of a material decreases. For example, the diameter of the smallest round bar necessary to measure *plane-strain fracture toughness*,  $T_{cs}$ , of steel, with a yield strength of 300,000 psi, would be less than 0.2 in. whereas the diameter necessary for a bar of steel with a yield strength of 150,000 psi, would exceed 5 in. [40].

In order to minimize specimen dimensions, thereby making most effective use of available test materials and equipment, types of specimens have been developed in which the length of an artificial crack is an appreciable fraction of the overall specimen dimensions. Sufficiently accurate expressions, obtained by mathematical and experimental methods, have been developed for several useful specimen types by SRAWLEY and BROWN [40].

Experiments [40] have shown that  $T_c$  decreases with specimen thickness, and becomes constant when specimen thickness increases to such an extent that the specimen is essentially under plane-strain conditions. The  $T_c$  value obtained under plane-strain conditions will be designated  $T_{cs}$  and is the lowest possible value of  $T_c$  for a material.

Details of the procedure used for determining fracture toughness of Chelmsford granite are given elsewhere [25]. Beams of granite were used for the tests. The crack in each beam specimen consisted of a saw cut of 0.005 in. width and of various depths. Four specimens were tested for each of the three quarry directions. The four specimens for each direction were the same, except crack lengths were cut to depths of 0.125, 0.250, 0.375 or 0.500 in.

A displacement gage [25] was designed to measure the widening of the crack as the beam specimen was bent by an applied load. The lengthening of the crack was correlated experimentally with the widening of the crack. A typical load-widening or load-displacement curve is shown in Fig. 9. The crack extended linearly up to a value corresponding with point A

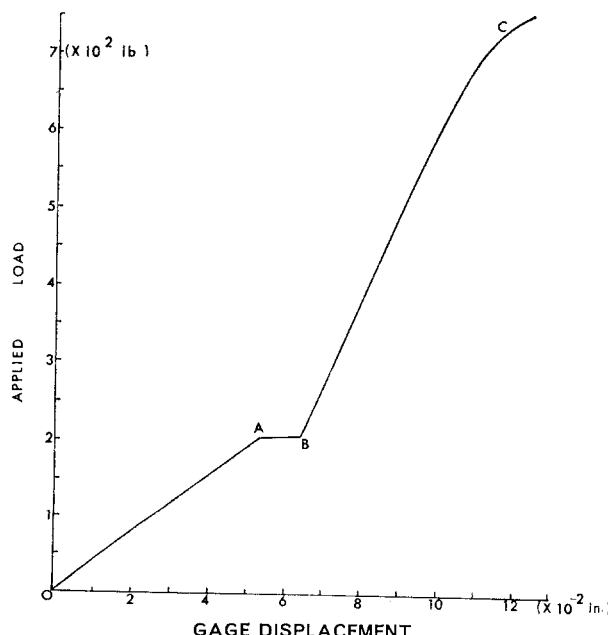


FIG. 9. Relation between load applied to beam specimen and widening of open end of artificial crack in fracture toughness test of Chelmsford granite.

TABLE 4. PLANE-STRAIN FRACTURE TOUGHNESS OF CHELMSFORD GRANITE

Sample no.	Crack length (in.)	Fracture toughness (psi in <sup>4</sup> )		
		Rift*	Grain	Hardway
1	0.125	644	582	501
2	0.250	454	638	450
3	0.375	464	426	479
4	0.500	560	449	545
Averages:		530	524	493

\* For example, plane of original crack parallel to rift.

in Fig. 9 after which the crack propagated slightly nonlinearly to complete rupture (point C). The value of  $T_c$  calculated from the displacement and the corresponding load for point A is the plane-strain fracture toughness,  $T_{cs}$ , of Chelmsford granite [40].

Table 4 shows the results of the tests with beam specimens of Chelmsford granite. The average values for the three directions are 530, 524 and 493 psi-in<sup>4</sup> parallel to the rift, grain and hardway directions, respectively. Thus, fracture toughness varies by as much as about 7.5 per cent in the different quarry directions whereas the Young's moduli vary by 29 per cent, the Brazilian tensile strengths vary by 30 per cent and the uniaxial compressive strengths vary by 9–13 per cent in the three quarry directions. Fracture toughness for Chelmsford granite is relatively constant and might be considered to be a physical property of the granite.

### 3. DEFORMATION OF CYLINDRICAL SURFACES OF SPECIMENS AND STRESSES WITHIN SPECIMENS SUBJECTED TO UNIAXIAL LOADING

Compression tests of circular cylinders of rock are performed routinely in order to determine constants in a fracture criterion, such as cohesion and friction of a Coulomb material, and in order to determine which fracture criterion describes most closely the behavior of a rock. The resulting criterion and constants are always based on the assumption of uniform stress distribution within the specimens (for example see [4, 41]). It is obvious that use of a fracture criterion or of constants derived by assuming a uniform stress distribution, yet applied to stress conditions known to be nonuniform, would be thoroughly misleading and confusing. Nevertheless, this is exactly what has happened for many years.

Some experimental rock mechanists have recognized that, in specimens under compression, the stress distributions are seldom uniform. The nonuniformities usually are blamed on end friction, so that various lubricants, such as graphite, silicon spray and teflon sheets have been used to reduce friction between the specimen and the testing platens [16]. Others have tried to reduce nonuniformity by modifying the shape of the specimen [18, 30]. But, so far, only one has demonstrated that he has actually obtained a uniform distribution of strains on surfaces of his specimens [25].

#### 3.1 Deformation of cylindrical surfaces of specimens subjected to various end-boundary conditions

PENG [25, 26] has investigated the stress distributions in samples in detail. He points out that there are two primary causes of nonuniform loading in specimens. One factor is friction

between the end of a specimen and the platens of the loading machine. In compression testing of a cylindrical specimen, for example, the specimen tends to expand radially as it shortens longitudinally. Frictional constraint at the planes of contact between the cylinder and the loading machine tends to prevent expansion. Thus, the sample becomes slightly barrel-shaped and the sample ends are subjected to shear stresses [Fig. 10(a)]. The other factor is the relative rigidity of the sample and the platens of the loading machine, or of the sample and the inserts placed between the sample and the platens. As noted above, the specimen tends to expand radially as it shortens. Now, if the platens of the loading machine were able to expand laterally as much as the specimen, there would be no tendency for the

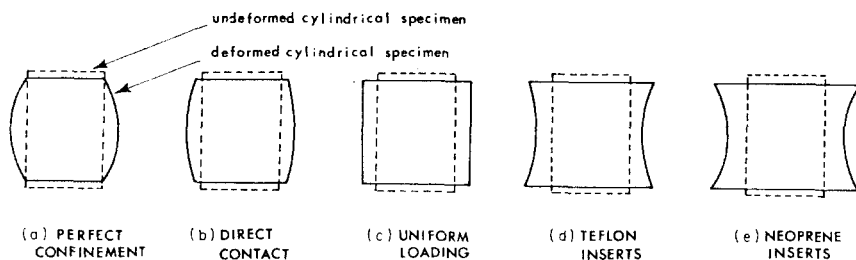


FIG. 10. Types of deformation recognized by measuring strains on surfaces of specimens of drill steel and Chelmsford granite deformed under various end-boundary conditions.

sample to become barrel-shaped. Rather, the specimen would be deformed uniformly. On the other hand, if the platens expand either more or less than the specimen, the loading is nonuniform. This relative rigidity is the most important factor because if the relative rigidities are equal, the amount of friction between specimen and platens or the inserts is irrelevant; there can be no frictional stresses if the sample and the platens expand the same amount. On the other hand, if the sample and the platens or inserts have different rigidities, the stresses in the sample will almost certainly be nonuniform. PENG [25] found that there is sufficient friction between specimens and relatively low-friction teflon inserts to significantly alter stress distributions within specimens. Therefore, the best experimental procedure for obtaining uniform loading is to experimentally select inserts that have the same rigidity as the specimens being tested.

PENG [25, 26] tried a variety of inserts, placed between specimens and the loading platens, in order to find empirically an end-boundary condition that produced uniform loading in specimens of Chelmsford granite. The types of inserts and the resulting deformations of the cylindrical surfaces are indicated in Fig. 10. He mounted five strain gages to measure vertical strains and seven gages to measure circumferential strains at various heights on the cylindrical surfaces of the specimens. He made similar measurements with samples of drill steel as well as Chelmsford granite in order to detect spurious results caused by inhomogeneities or anisotropic properties of the granite. For further details of his techniques and for the full set of data, see PENG [25].

Some of Peng's results are shown in Figs 11(a)-11(c). Figure 11(a) shows vertical strain,  $\epsilon_v$  and circumferential strain,  $\epsilon_\theta$ , for specimens of granite *g* and drill steel *s* which were in

*direct contact* with the platens *a* of the loading machine. Friction between the end surfaces and the platens and the tendency for the specimen to expand cause the specimen to bulge outward at the middle. The strain in the middle third of the specimen is nearly uniform. The values of vertical strain show that granite and steel specimens both strain more near end surfaces than at midheights.

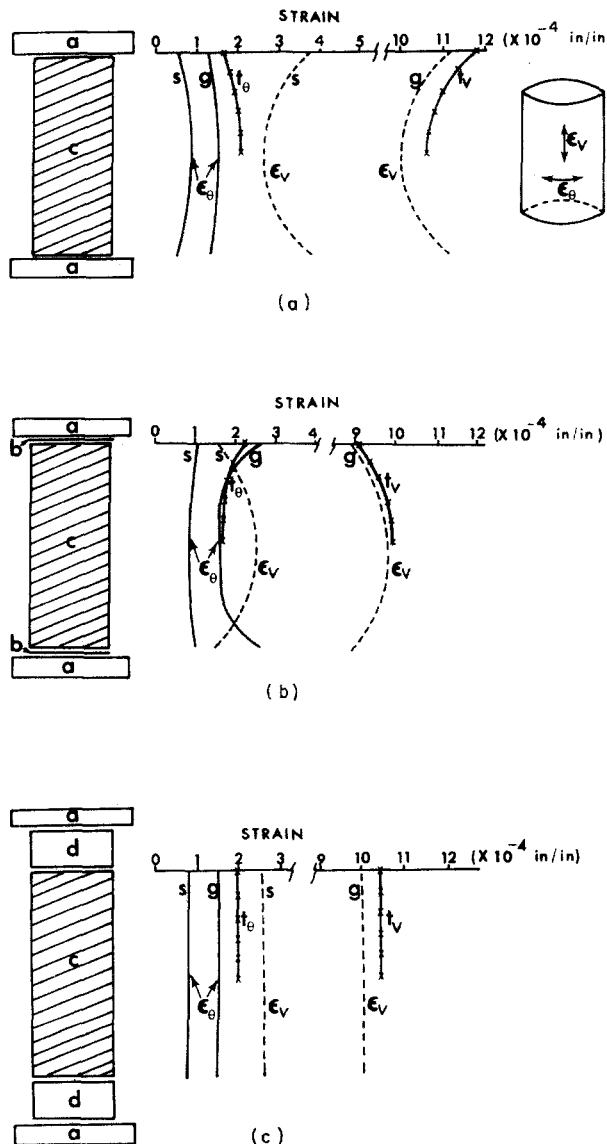


FIG. 11. Strain profiles of cylindrical surfaces of specimens of Chelmsford granite and drill steel. *a*—machine platen, *b*—Teflon sheet, *c*—specimen, *d*—steel insert, *s*—steel specimen, *g*—granite specimen,  $\epsilon_v$ —vertical strain,  $\epsilon_\theta$ —circumferential strain,  $t_v$ —theoretical vertical strain,  $t_\theta$ —theoretical circumferential strain.

- (a) Sample in *direct contact* with loading platens.
- (b) *Teflon inserts* placed between ends of sample and loading platens.
- (c) *Uniform loading* achieved by placing steel disc 1½ in. in length between ends of sample and loading platens.

Figure 11(b) shows strain where *teflon inserts*, or sheets of teflon, 0·005 in. thick and with the same diameter as the ends of the specimen, were inserted between the end surfaces and the platens. The result is completely different! The end surfaces expand radially more than the middle of the specimen. The vertical strains also have opposite patterns; the vertical strain at midheight on the cylindrical surface of a specimen with teflon inserts is greater than the vertical strain near the end surfaces.

Strains of specimens where discs of drill rod,  $1\frac{1}{2}$  in. in diameter and  $1\frac{1}{4}$  in. long, were inserted between the specimen and the platens are shown in Fig. 11(c). These discs of steel produced the most nearly uniform strain distribution of all possibilities examined by PENG [25]. This system will be called *uniform loading* in the following pages.

The other boundary conditions, illustrated in Fig. 10, will not be described in detail here. It is sufficient for our purposes to note that the condition of *perfect confinement* was approached by tightening narrow hose clamps around each end of specimens and the condition of *neoprene inserts* involved insertion of wafers of neoprene rubber,  $\frac{1}{16}$  in. thick, between the sample ends and the loading platens.

One might suggest inserting discs of the same material as the specimen. This is useful for measurements of elastic constants of the material, but is not ideal for fracture testing, because the discs usually fail first and experience shows that fractures tend to terminate within the discs, at the contact plane between the end surfaces of the specimen and the discs.

Deformations of cylindrical specimens tested with neoprene rubber and teflon inserts are shown schematically in Figs 10(d) and 10(e). The cause of the deformations shown is due to radial expansion of the teflon and neoprene inserts and to the accompanying shear stress transmitted from the inserts to the end surfaces of the specimens. The angles of internal friction for teflon and neoprene, required to cause the deformations observed, have been calculated to be about  $1^\circ$  and  $5^\circ$ , respectively. Inspection of the teflon and neoprene sheets after tests shows that the circumferential edge of each teflon sheet became noticeably thinner, whereas the inner area seemed to retain its original thickness. The neoprene tends to extrude from between the specimen and machine platens as soon as axial load is applied. The amount of radial flow of neoprene is higher than that of teflon. For teflon, the flow was recoverable at low axial loads, but permanent at high loads, whereas for neoprene, the flow was permanent even at low axial loads.

According to the extensive series of tests performed by PENG [25, 26], it clearly is important to examine both the vertical and the circumferential strain distributions within specimens tested in compression. It is poor testing procedure to put a specimen directly against a platen which has a larger diameter than the specimen. Teflon has a very low friction angle, but its use does not guarantee a uniform stress distribution, as has been claimed by some investigators, for example HARDY JR[42]. Indeed, the teflon sheet causes that part of the specimen which is in immediate contact with it to expand radially.

In order to induce a uniform strain distribution within a specimen subjected to uniaxial compression, it is desirable to use inserts made of a material of the same diameter as the specimen. The overall length of the inserts should be at least equal to the diameter of the specimen. For each kind of rock, it may be necessary to perform tests to analyze the uniformity of the strain distribution in terms of both circumferential and vertical strains. Then compressive strengths can be measured, perhaps with some meaning.

If Peng's experiments and analyses do nothing more, they should make it crystal clear that the performance of meaningful laboratory uniaxial tests of rocks is much more complicated than is usually believed, and that end conditions must be considered.

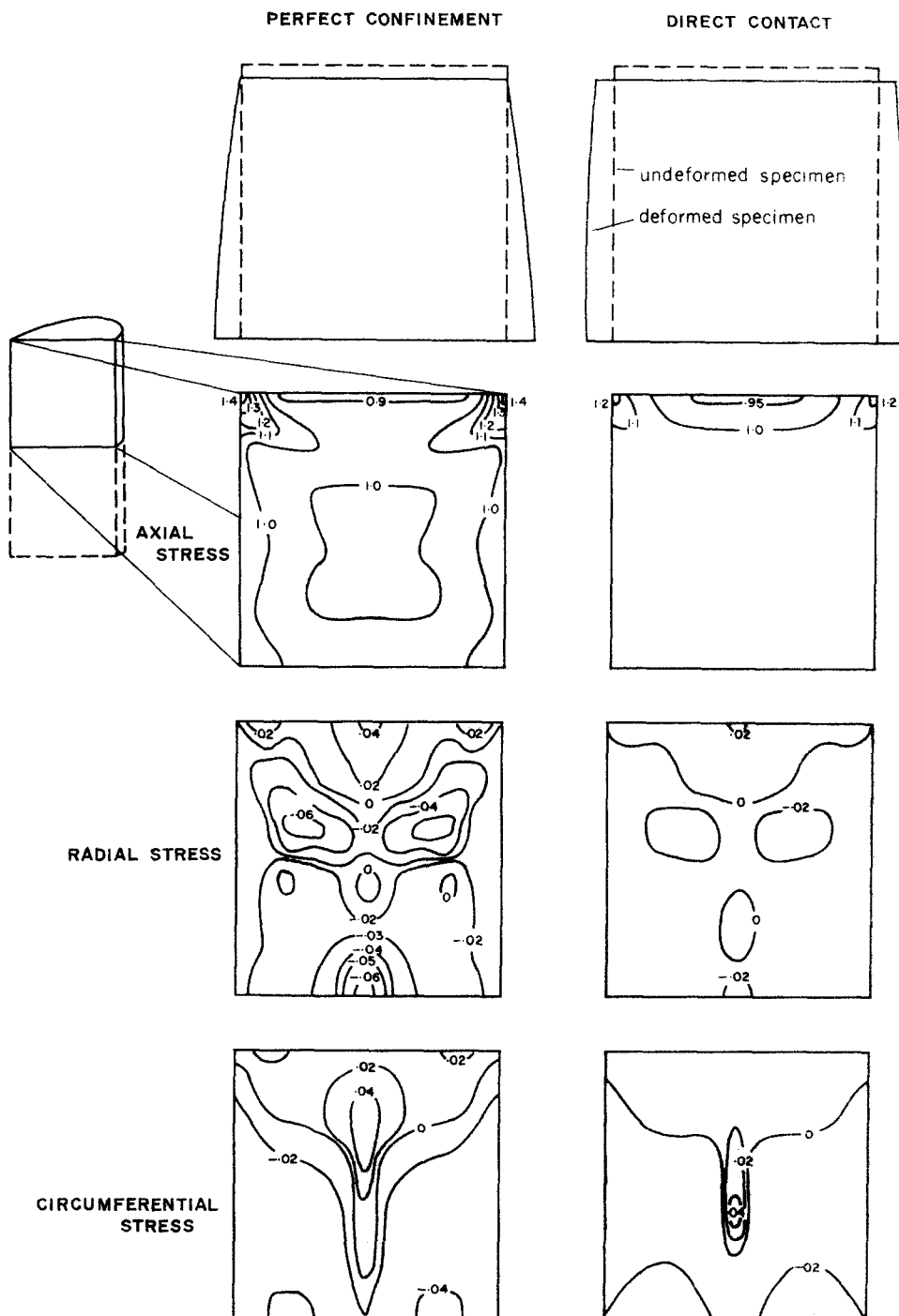
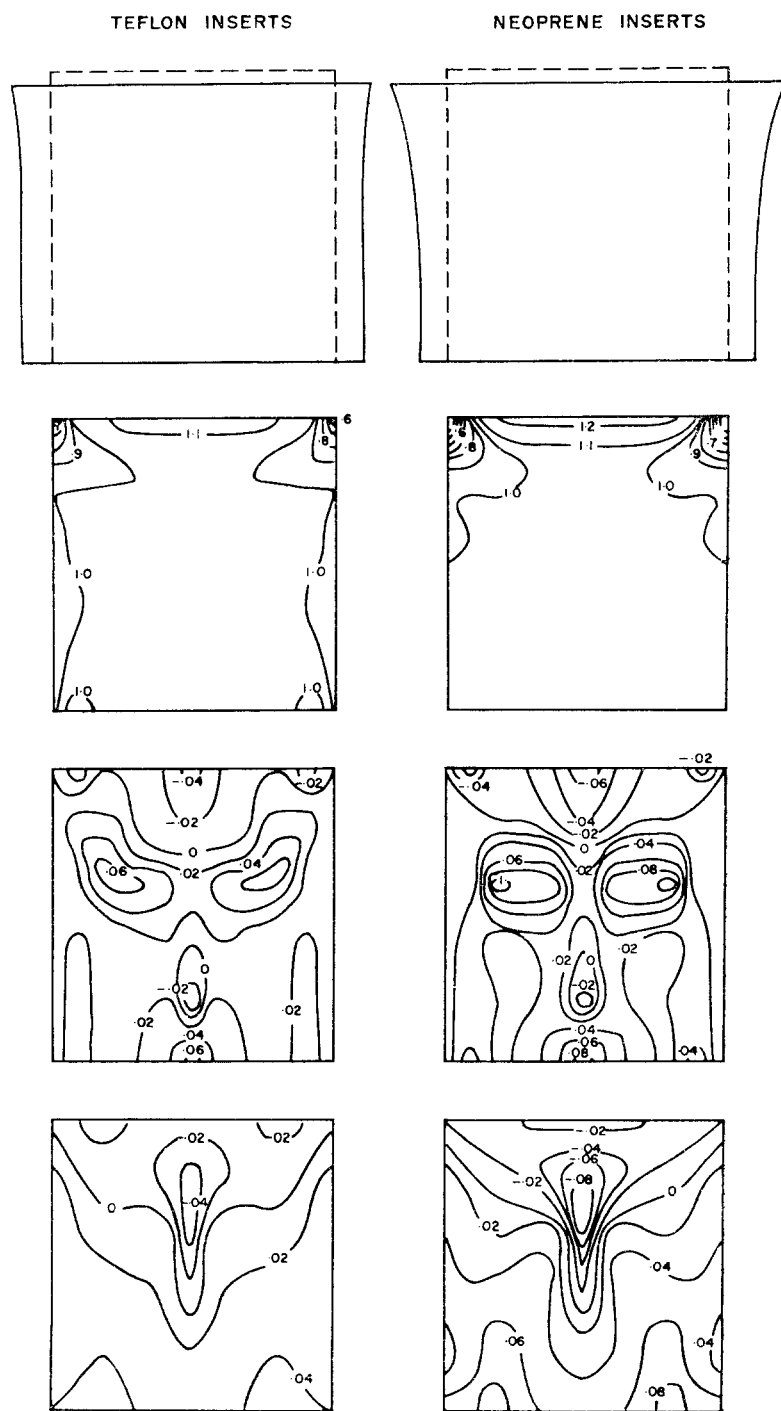


FIG. 12. Contour maps of stress concentrations within specimens of Chelmsford granite subjected to various end-boundary conditions. Only the upper halves of specimens are shown.

FIG. 12 (*cont.*)

### 3.2 Theoretical distributions of stresses within samples of Chelmsford granite subjected to various end-boundary conditions

PENG [25, 26] has derived a new theoretical solution for stresses within cylindrical specimens loaded uniaxially under the types of end-boundary conditions illustrated in Fig. 10. In addition to the usual boundary conditions that shear and radial stresses vanish at cylindrical surfaces and that ends of specimens remain plane before and during loading, Peng has introduced two new conditions. One is that the ratio of the circumferential strain at each end surface and at midheight of the specimen is known and the other is that the ratio of the vertical strains at these two places is known. (See PENG [25, 26] for details of the derivations.)

Figure 12 shows contour maps of stress distributions within uniaxially-loaded specimens subjected to various end-boundary conditions. All stresses are symmetrical with respect to the midplane of specimens, so that only the upper halves of specimens are shown. The distribution of various stress components for each boundary condition are arranged in a column. The first row of each column is a schematic illustration of the shape of the deformed specimens for each boundary condition. The second through the fourth rows show distributions of axial, radial and circumferential stresses, respectively.

*Axial stress distribution.* The first row of the first column in Fig. 12 is a contour map of axial stress concentrations for the boundary condition of perfect confinement. The maximum concentration is +1.44 and occurs at the corners and the minimum concentration occurs at the center of the end surface and is +0.89. The axial stresses at, and close to, the end surface are lower than those for most of the remainder of the specimen.

The first row of the third column in Fig. 12 is the contour map of axial stress concentrations for the teflon insert boundary condition. It has a maximum at the center of the end surface with a value of +1.1 and minimum of +0.59 at the corners.

*Radial stress concentrations.* The third row of Fig. 12 shows contour maps of radial-stress concentration for various boundary conditions.

The third row of the first column is the radial-stress concentration for perfect confinement. Both compressive and tensile radial stresses occur. The maximum compressive radial stress, with a value of +0.04, is at the center of the end surface. The radial stress reaches the highest tensile stress of -0.06 at about  $2H/5$  from the end surfaces. At the midplane, all radial stresses are tensile.

The third row of the third column in Fig. 12 shows the contour map for the radial-stress concentration for teflon inserts. Again, both tensile and compressive radial stresses occur. The highest tensile stress occurs at the center of the end surface and has a value of -0.04. The radial stress increases to the highest compression of 0.06 at about  $2H/5$  from the end surface and at the center of the midplane.

*Circumferential stress concentrations.* The fourth row in Fig. 12 shows circumferential stress-concentration contour maps for various boundary conditions.

The fourth row of the first column shows circumferential stress concentrations for perfect confinement. Both compressive and tensile circumferential stresses occur within the specimen. The largest compressive stress concentration is +0.05 and occurs along the axis of the specimen, between distances of  $H/4$  and  $2H/5$  from the end surface. The largest tensile stress concentration is -0.05 and occurs at the midplane, at a distance of about  $R/2$  from the center of the specimen.

The fourth row of third column shows circumferential stresses in samples with the teflon inserts boundary condition. The largest tensile stress is -0.05 and is located along the axis of the specimen at a distance of between  $H/4$  and  $2H/5$  from the end surface. The maximum

compressive circumferential stress concentration is  $+0.05$  and occurs at  $R/2$  from the axis, at midheight in the specimen.

*Summary of stress distributions.* Figure 12 shows that there are certain common places of high stress concentration and that their tendencies can be generalized:

1. 'Uniaxially loaded' specimens in most laboratory tests are actually triaxially stressed. The stresses are different in different directions and they vary from point-to-point within the specimen. It is clear that the state of axial stress within a rock specimen loaded uniaxially is not simply the force applied to each end of the specimen divided by the area of each end.

2. The stress concentration contour maps for each type of stress, such as radial or axial are similar in form for all kinds of end-boundary conditions tested.

3. For the boundary conditions of perfect confinement and direct contact, the absolute values of maximum and minimum stress concentrations and the stress gradients increase with increasing friction. Therefore, highly nonuniform stress distributions are expected for perfect confinement. Stresses become more uniformly distributed as frictional constraint decreases. The magnitudes of radial and circumferential stresses decrease as the expansion of the end platens approaches that of the specimens. When the expansions are equal, of course, the axial stress concentration reduces to one throughout the specimen; this is what we mean by a uniform stress distribution. For teflon inserts and neoprene inserts end-boundary conditions, involving platens or inserts that expand more than the specimen does, the absolute values of maximum and minimum stress concentrations decrease. Also, the rate of change of stress increases as the expansional effects of the end inserts increase. Therefore, the more expansive the end inserts, the more nonuniform the stress distributions within specimens. This phenomenon is true for all components of stress.

4. Except for the uniform boundary condition, both compressive and tensile radial and circumferential stresses simultaneously exist. For perfect confinement and direct contact boundary conditions, compressive radial and circumferential stresses occur in an area quite similar in form to an upside-down triangle whose base is the end surface of the specimen, and whose height is about  $H/3$  for radial stresses and  $H/2$  for circumferential stresses. The rest of the area has tensile stresses. Teflon inserts and neoprene inserts boundary conditions give opposite results. Tensile stresses occur in the triangular area at the end surfaces and compressive stresses occur in the rest of the area.

#### 4. DISTRIBUTION AND GROWTH OF CRACKS IN SAMPLES OF CHELMSFORD GRANITE SUBJECTED TO VARIOUS END-BOUNDARY CONDITIONS

Thus far, we have discussed the defects, including microcracks and mica flakes, in specimens of Chelmsford granite, and the theoretical stress distributions within elastic specimens subjected to various end-boundary conditions. This section is concerned with investigation of initiation and propagation of small cracks from preexisting defects in the granite. It is based on study of cut sections of rock cores and analyses of theoretical stress distributions in elastic cylinders.

In the following pages, only *G*-specimens (Fig. 1), the end surfaces of which are parallel to the grain plane, will be investigated. The results presumably are representative of Chelmsford granite in general because all specimens tested, regardless of orientation, failed in the same mode under the same boundary condition.

##### 4.1 Crack distributions developed under various end-boundary conditions and uniaxial loading

Granite specimens were loaded to various levels, unloaded and then cut lengthwise into halves. The cut surfaces were polished with 800-gr. emery powder. One half was used for

making a thin section, and the other half was inspected with an  $8\times$  binocular microscope. Only the upper half of the specimen was examined to determine the crack pattern. The cut face of the upper half of the specimen was divided into 32 units by means of a square grid. Figure 13 shows grid dimensions and assigned grid numbers. For example, grid number one covers the area between a line that is a distance  $H/4$  from the end surface and a line that is a distance  $D/4$  from the left-hand edge of the specimen. The number of cracks and their lengths were measured and recorded for each square or grid. The cracks in loaded specimens tend to develop preferentially in certain areas, depending on boundary conditions, and this pattern of preferential development is called the *crack pattern*.

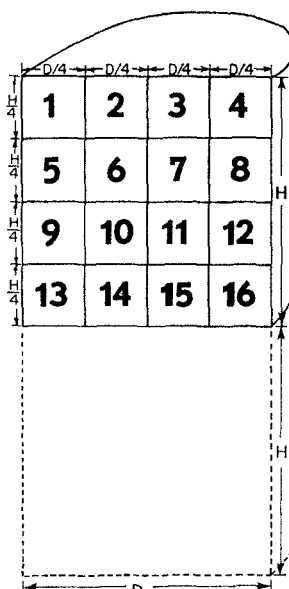
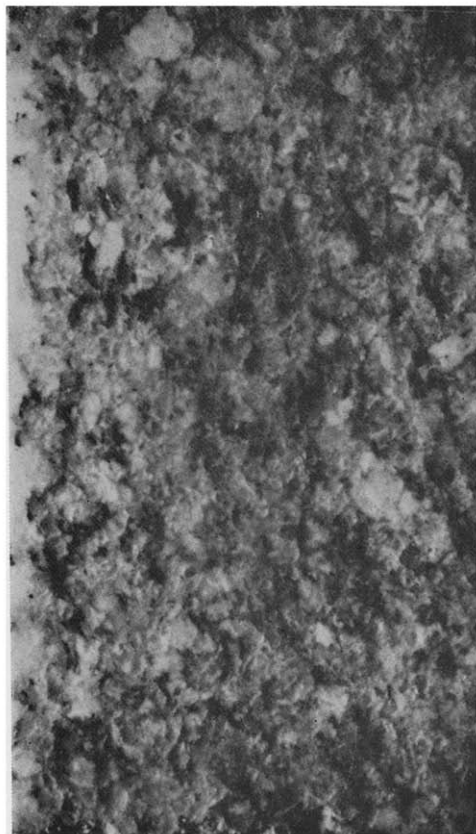


FIG. 13. Cross-sectional view of cylindrical specimen, showing cut surface, grid dimensions and grid numbers.  $H$  is the half height and  $D$  is the diameter of the specimen.

Cores of granite were drilled from blocks and the cores were cut into cylindrical specimens with length-to-thickness ratios of two. One end of each core was saved for study of crack patterns in specimens that were not loaded. Figure 14(a) is a photograph of a cut surface of a typical specimen, showing an initial crack pattern. The larger cracks have been traced in Fig. 14(b). The cracks are preferentially oriented parallel or subparallel to the rift and grain planes [see Fig. 3(c)]. The average crack density is 18 per grid of  $0.17\text{ in}^2$ , or about  $106/\text{in}^2$  (Table 5). Figure 15(a) shows a contour map of a number of cracks within each grid, that is, of *crack density*. The crack density is relatively uniform, ranging from about 12 to  $22/0.17\text{ in}^2$ .

The other piece of each core was subjected to uniaxial loading. In specimens where the axial load reached the low value indicated by point *A* on the stress-strain curve shown in Fig. 16(c), there was no conspicuous growth of cracks, regardless of the kind of boundary condition imposed. A typical view of a cut specimen is shown in Fig. 16(a). The total number of microcracks in each grid is listed in Table 5 and is shown in the contour map in Fig. 15(b). The average crack density is  $19.5/\text{grid}$ , or  $11/\text{in}^2$ .



(a)

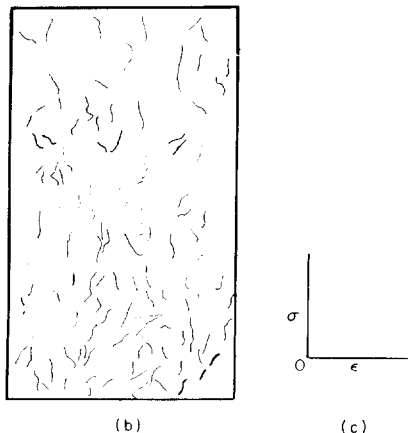
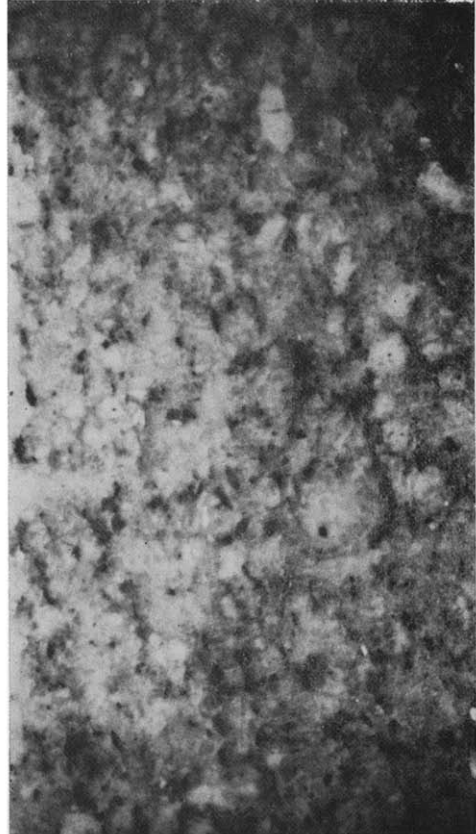


FIG. 14. Typical cut section for specimen that was not loaded.

RM f.p. 60]



(a)

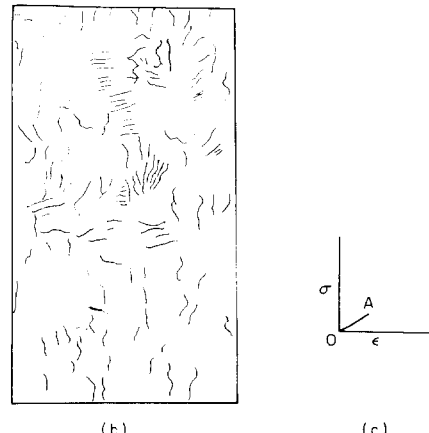
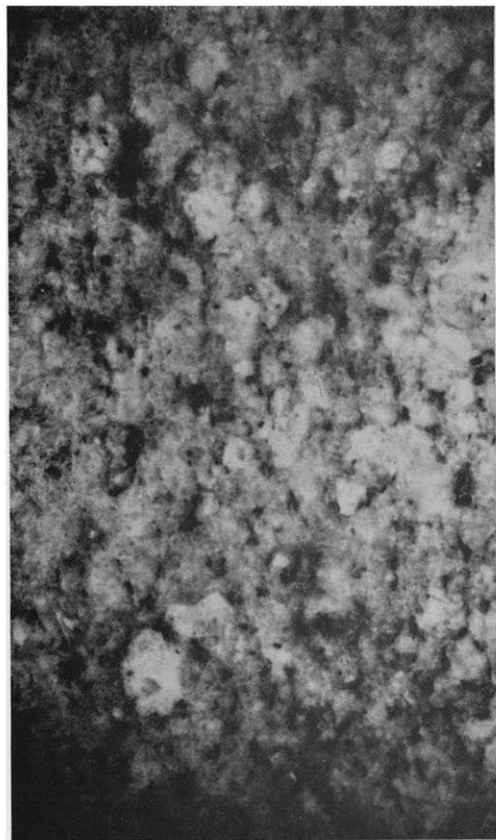
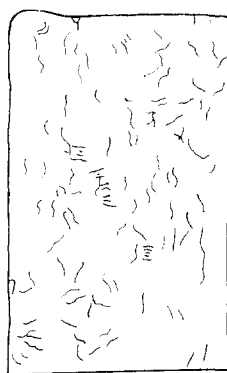


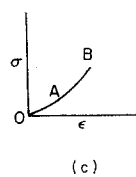
FIG. 16. Some of cracks visible in cut section of granite specimen loaded to a low level.



(a)

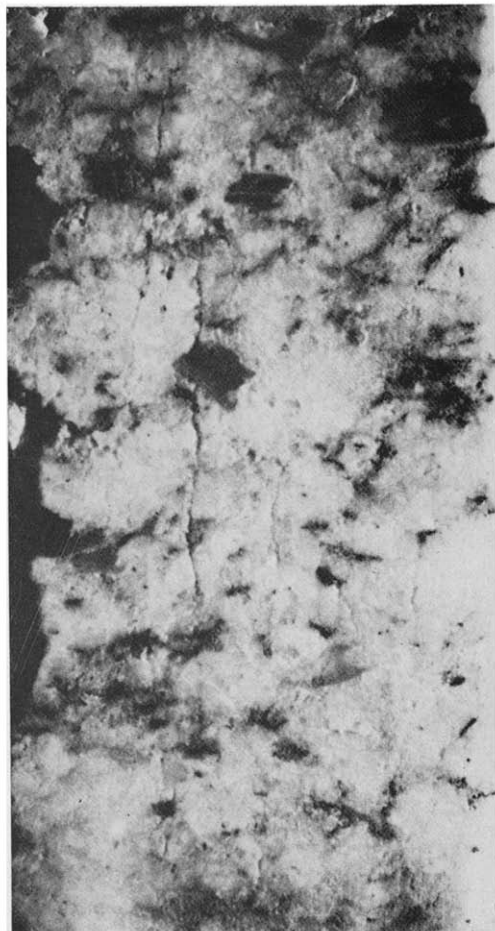


(b)

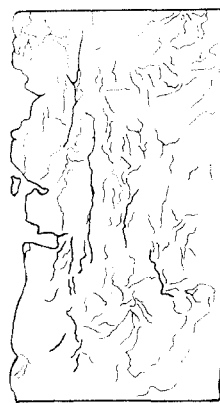


(c)

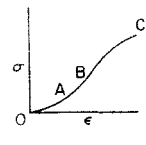
FIG. 17. Cut section of specimen of granite loaded to an intermediate level, showing some of the cracks.



(a)



(b)

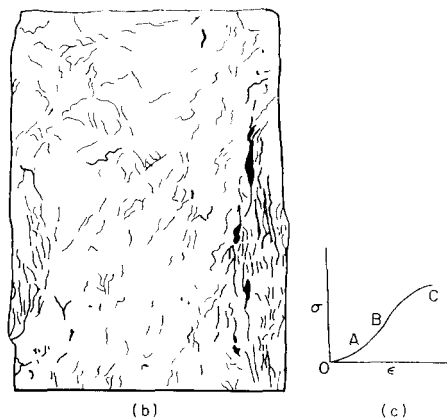


(c)

FIG. 18. Cracks that developed in specimen of granite under end conditions of *uniform loading*. Loading was stopped immediately before failure occurred.



(a)



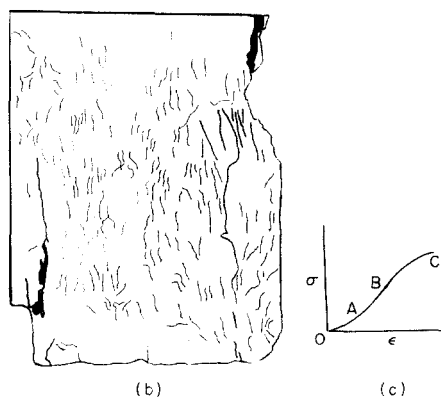
(b)

(c)

FIG. 19. Cracks in upper two-thirds of granite specimen that was subjected to end conditions approaching *perfect confinement*. Loading stopped immediately before failure occurred.



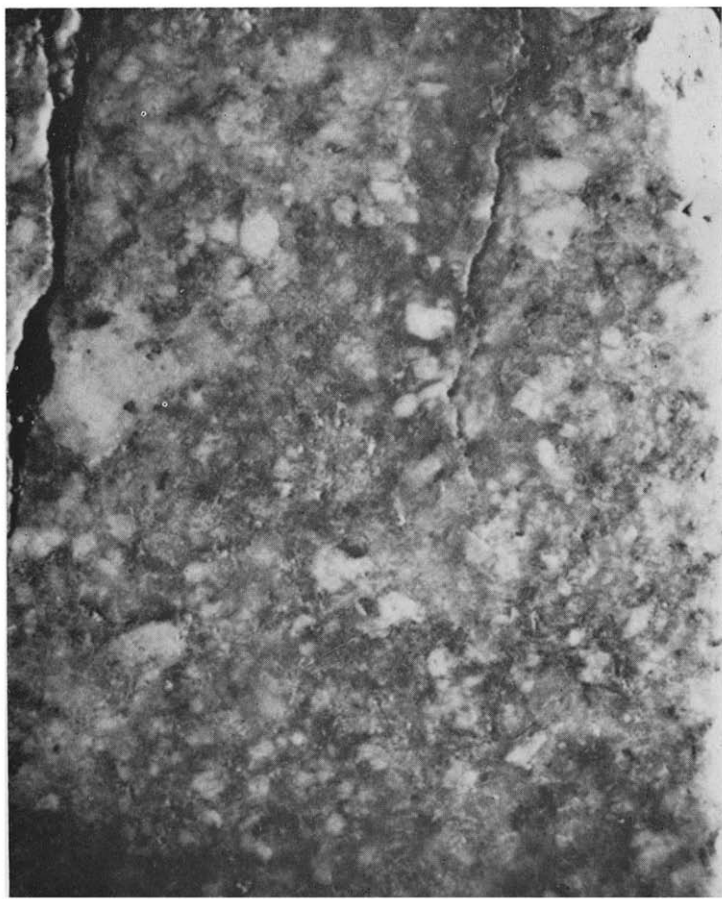
(a)



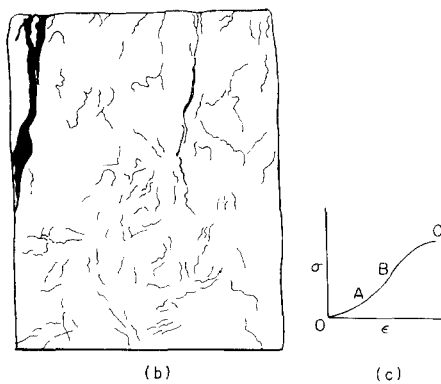
(b)

(c)

FIG. 21. Cracks in upper two-thirds of specimen of granite that was loaded nearly to failure under end conditions of *direct contact* with the machine platens.



(a)



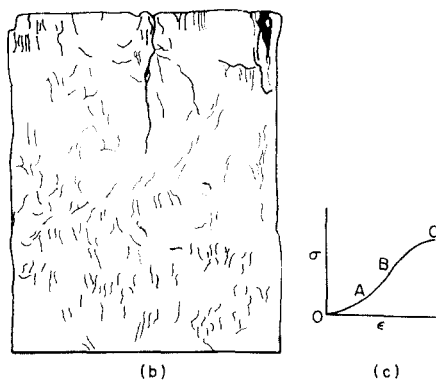
(b)

(c)

FIG. 22. Cracks in upper two-thirds of specimen of granite subjected to *teflon inserts* boundary conditions  
Loading stopped immediately before failure occurred.



(a)



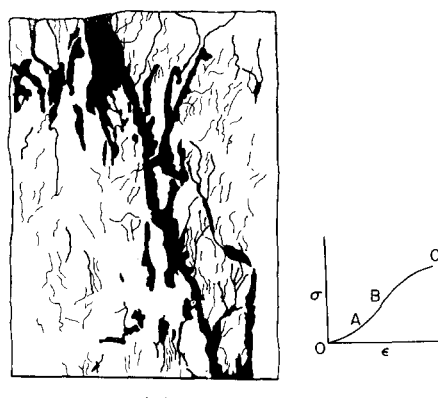
(b)

(c)

FIG. 23. Cracks in upper two-thirds of specimen of granite that was loaded nearly to failure under end conditions of neoprene inserts.



(a)



(b)

(c)

FIG. 24. Cracks and gross fracture plane in upper two-thirds of specimen of Chelmsford granite subjected to end conditions of direct contact and a confining pressure of 5000 psi ( $3.45 \times 10^7 \text{ N/m}^2$ ).

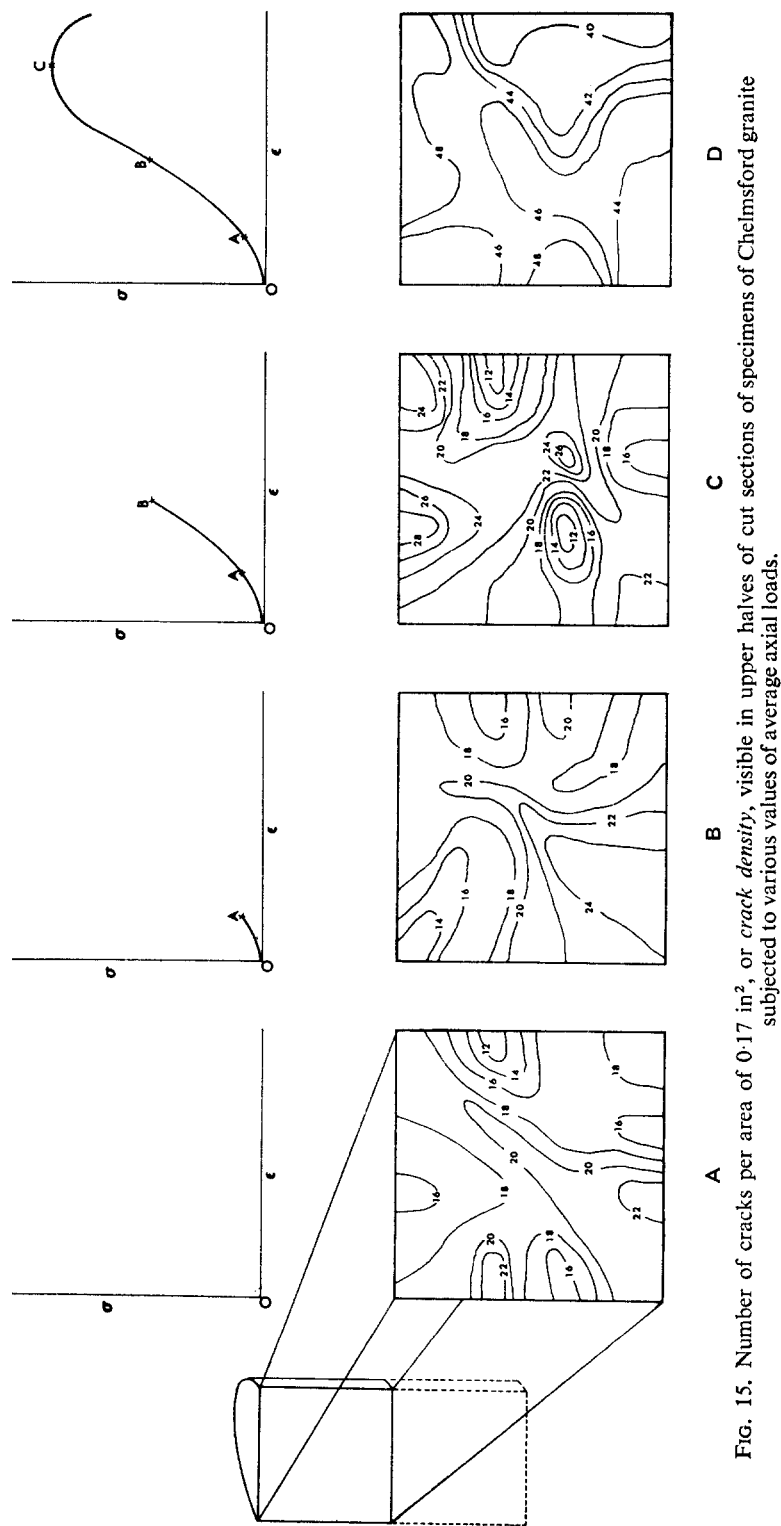


FIG. 15. Number of cracks per area of  $0.17 \text{ in}^2$ , or crack density, visible in upper halves of cut sections of specimens of Chelmsford granite subjected to various values of average axial loads.

Specimens loaded to the value indicated by point *B* on the stress-strain curve shown in Fig. 17(c) were studied to detect crack growth. A typical specimen is shown in Fig. 17(a). Again, there was no significant crack growth [Fig. 15(c)]. The average crack number was 20·3/grid or 120/in<sup>2</sup> (Table 5).

The stress-strain curve becomes definitely nonlinear at stresses beyond the value indicated by point *B* in Fig. 18(c). Specimens loaded to point *C* were inspected to study crack growth (Fig. 18). The crack patterns are different for different boundary conditions, so that results for each boundary condition will be discussed separately.

*Uniform loading.* Figures 18(a) and 18(b) show crack development in a specimen loaded with the uniform end-boundary condition. Figure 18(a) is a photograph of the cut surface and, for ease of identification, some of the larger cracks visible in the photograph have been traced in Fig. 18(b). Cracks are traced as lines, the thicknesses of which represent the widths of the cracks. The long cracks are clearly preferentially oriented parallel to the axis of the specimen. The number of cracks in each grid is quite uniform and the average number is 44·8/grid or 264/in<sup>2</sup> [Table 5 and Fig. 15(d)]. The most obvious change in contour maps of crack density, shown in Figs 15(c) and 15(d), is that the number of cracks essentially doubles as the axial load increases from the value indicated by point *B* to the value indicated by point *C* on the stress-strain curve [Fig. 18(c)].

*Perfect confinement.* Figure 19 shows the crack pattern in a specimen of Chelmsford granite subjected to a boundary condition approaching that of perfect confinement, achieved by tightening a narrow hose clamp around each end of the specimen. As before, the specimen was loaded to point *C* on the stress-strain curve. More cracks lengthened in the middle of the specimen, near the base of Fig. 19(b), than near the end surface, at the top of Fig. 19(b). The number of cracks visible within each 0·17 in<sup>2</sup> area is shown by means of a contour map in Fig. 20(a). The original data are in Table 5. The average crack density is 36·4/grid or about 214/in<sup>2</sup>. Thus, crack density of visible cracks in specimens loaded to point *C* under conditions of perfect confinement is approximately double that in specimens that were not loaded [Fig. 15(a)]. Further, the contour map shows that more cracks initiate and grow near midheight in the specimen than at the end surfaces.

*Direct contact.* Figures 21(a) and 21(b) show the crack pattern for a specimen subjected to the boundary condition of direct contact. One long crack extends from the upper-right end surface, parallel to the axis of the specimen, and terminates at about  $H/3$  from that end surface. Other long cracks are visible in the figures. The crack densities are shown in Fig. 20(b) and in Table 5. The average crack density is 33·3/grid or 190/in<sup>2</sup>. The pattern of cracks is asymmetric, but it seems ideally to consist of a band of high crack density looping from each corner to a distance of about  $H/2$  from the end surfaces (see last row of figures in Fig. 20). The crack densities are low in grids 2, 3 and 13 [Fig. 20(b)]. Grids 6 and 7 have the highest crack densities of 55 and 54, respectively (Table 5). The grids at the corners have high crack densities also.

*Teflon inserts.* Figures 22(a) and 22(b) show crack development for a sample of Chelmsford granite loaded under boundary conditions of teflon inserts. Most of the cracks preferentially grew near the end surface (top in Figs 22 and 20(c)) and most of them are parallel to the axis of the specimen. Two long cracks near the ends are especially evident in Fig. 22(b). The crack density for each grid is shown in Table 5 and a contour map of crack density is shown in Fig. 20(c). The average crack density is 38·4/grid or 226/in<sup>2</sup>. The maximum number of cracks occurs in grids 2 and 3, with 52 and 54, respectively. The next highest densities

TABLE 5. CRACK DENSITIES WITHIN SPECIMENS OF CHELMSFORD GRANITE

Grid† no.	Crack density			Number of cracks in grid† with area of 0.17 in <sup>2</sup> Loaded to 'C'*					
	Not loaded	Loaded to 'A'*	Loaded to 'B'*	Perfect confinement	Direct contact	Uniform loading	Teflon inserts	Neoprene inserts	Triaxial‡ loading
1	18	14	22	24	40	45	31	26	46
2	15	19	29	17	15	50	52	47	48
3	18	20	15	15	13	40	54	49	52
4	19	19	25	20	52	51	39	31	44
5	23	19	19	34	37	46	37	39	34
6	17	14	23	32	55	46	44	40	49
7	21	20	21	25	54	47	48	43	51
8	12	15	10	40	39	40	39	32	30
9	15	22	18	53	13	49	33	33	30
10	20	25	11	50	45	46	35	32	47
11	17	18	27	48	40	41	39	44	49
12	17	20	22	39	24	41	32	38	31
13	21	24	23	48	17	41	28	30	29
14	22	25	20	50	28	44	40	25	42
15	16	20	16	41	26	49	34	27	40
16	19	18	19	46	35	40	30	23	34

\* See Fig. 15.

† See Fig. 13.

‡ These values are approximate (see text).

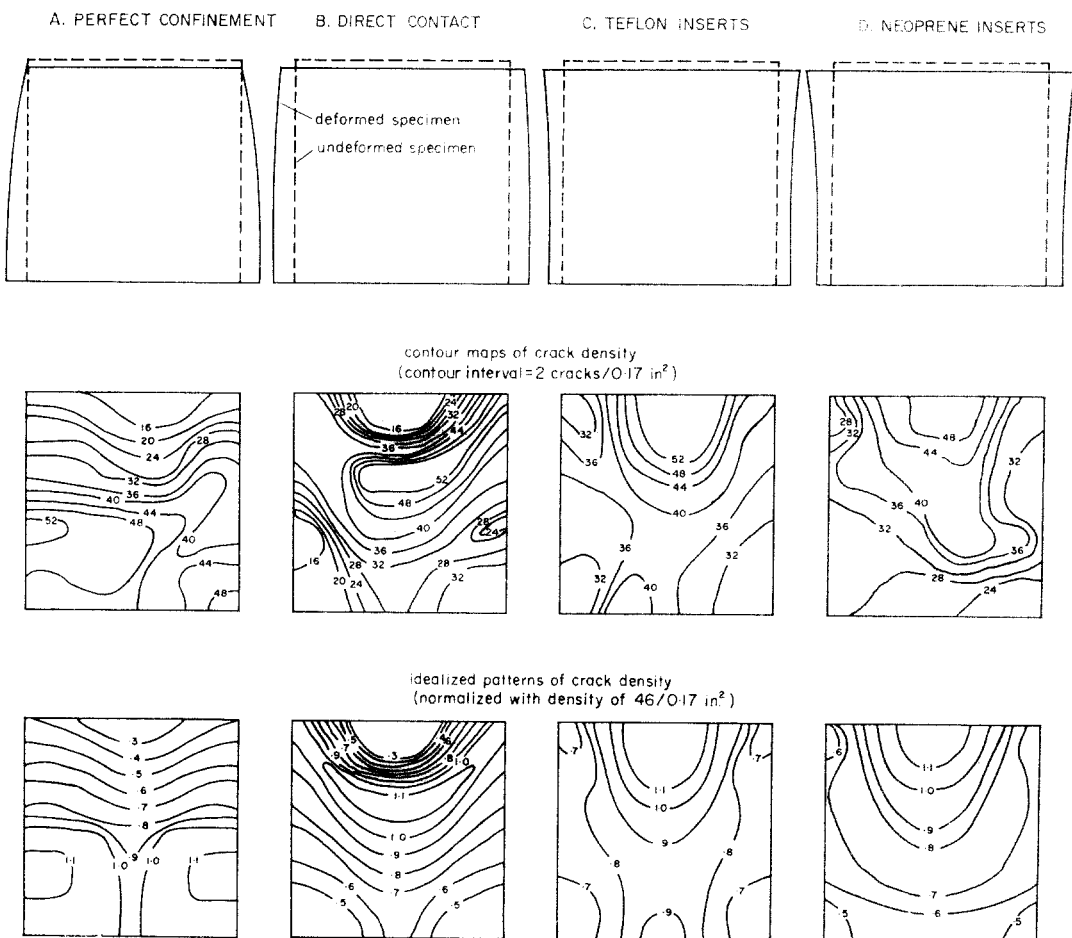


FIG. 20. Contour maps of crack density in upper halves of specimens of Chelmsford granite subjected to various end-boundary conditions. Upper row of figures shows deformed shapes of specimens. Middle row shows contour maps of crack densities, in units of numbers of cracks per area of  $0.17 \text{ in}^2$ . Lower row shows ideal contour maps of crack densities, deduced by studying theoretical stress distributions and the contour maps in the middle row, in units of  $46 \text{ cracks}/0.17 \text{ in}^2$ .

are in grid 6 with 44 and in grid 7 with 48. The areas of lowest density of cracks are near the cylindrical surface, at midheight in the specimen, within grids 13 and 16.

*Neoprene inserts.* Crack growth in a specimen subjected to the end-boundary condition of neoprene inserts was essentially the same as that for teflon inserts [see Figs 23 and 20(d)].

#### 4.2 Crack distribution developed under triaxial loading

Specimens were tested under the same end-boundary conditions in triaxial tests as in uniaxial tests. The end-boundary condition that produced uniform uniaxial loading did not produce uniform triaxial loading, however. Presumably, the nonuniformity is due to the testing technique. The boundary conditions of perfect confinement, direct contact, teflon inserts and neoprene inserts in triaxial loading showed the same distribution of surface strains as did their counterparts under uniaxial loading (Figs 10 and 11).

The crack pattern in a specimen subjected to direct contact and to 5000 psi ( $3.45 \times 10^7$  N/m<sup>2</sup>) confining pressure is shown in Figs 24(a) and 24(b). The specimen was highly fractured because the stiffening element used to arrest failure under uniaxial conditions would not fit into the triaxial chamber. Therefore, crack densities could not be determined accurately in specimens loaded triaxially. The crack density determined by study of the highly fractured specimen shown in Fig. 24(a) is about 40/grid or about 240/in<sup>2</sup> (Table 5).

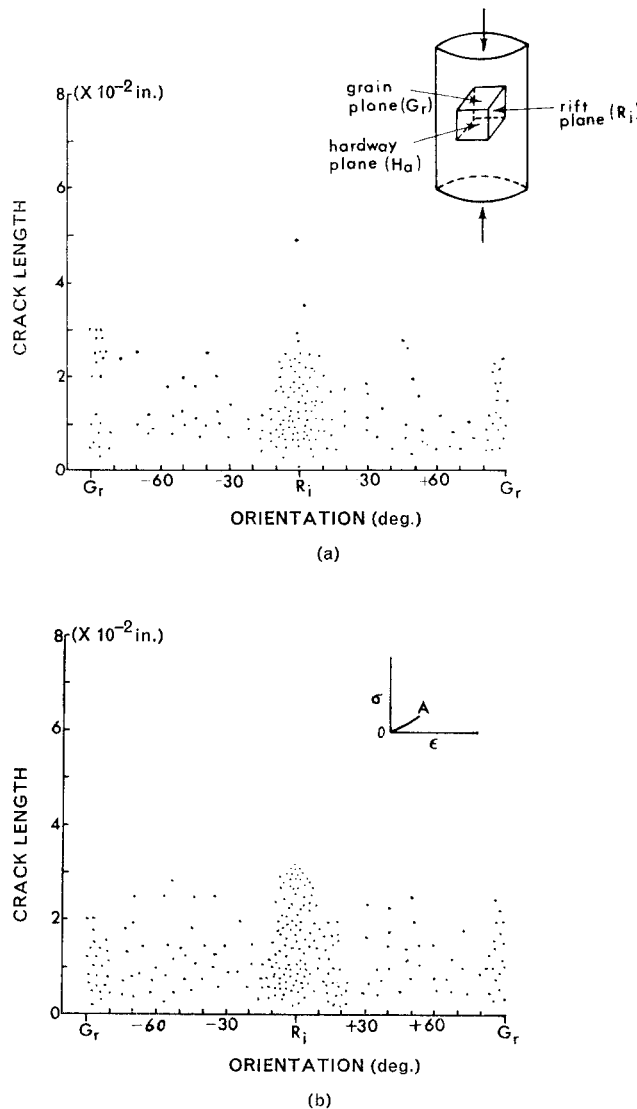


FIG. 25. Distributions of crack lengths relative to quarry directions in specimens of granite subjected to low values of axial load.  $R_i$  is rift plane.  $G_r$  is grain plane.

- (a) Crack-length distribution in specimen that was not loaded.
- (b) Crack lengths in specimen that was loaded to a low value.

#### 4.3 Crack lengthening

In addition to crack density, an important measure of crack growth is crack length. Thus, crack lengths were measured in the samples discussed in the preceding section. The average crack length at each stage of loading was compared with that for an original, unloaded specimen.

Crack length was measured with an  $8 \times$  binocular microscope and a vernier caliper, the sensitivity of which is about  $2.5 \times 10^{-4}$  in. Figure 25(a) shows the lengths of cracks in a specimen that was not loaded.  $Ri$  and  $Gr$  represent directions of rift and grain planes, respectively. Positive angles were measured clockwise from the rift plane to the crack plane; negative angles were measured counterclockwise. Among the 290 cracks measured, 70 per cent were concentrated on orientations within  $10^\circ$  of the rift plane and 15 per cent were within  $10^\circ$  of the grain plane. Crack lengths ranged from 0.002 to 0.05 in., with an average of 0.015 in.

Figure 25(b) shows the crack-length distribution for a specimen loaded to point *A* on the stress-strain curve. It was derived from the sample shown in Fig. 16. Of the 312 cracks measured, 60 per cent concentrated on orientations within  $20^\circ$  of the rift plane and 20 per cent concentrated around the grain plane. The crack lengths ranged from 0.001 to 0.045 in. and averaged 0.021 in.

Figure 26 shows crack lengths for a specimen loaded to point *B* on the stress-strain curve. It was derived from the specimen shown in Fig. 17. There are 325 length measurements: 75 per cent of them were within  $15^\circ$  of the rift plane and 7 per cent of them were within  $5^\circ$  of the grain plane. The crack lengths ranged from 0.005 to 0.03 in. with an average of 0.012 in.

Figures 27–31 show crack length distributions for specimens loaded to their ultimate strengths (point *C* in the stress-strain curve) under different boundary conditions. Different scales are used in the figures.

Figure 27 shows the crack-length distribution for a specimen under perfect confinement. Of the 582 cracks measured, about 80 per cent were located within  $10^\circ$  of the rift plane.

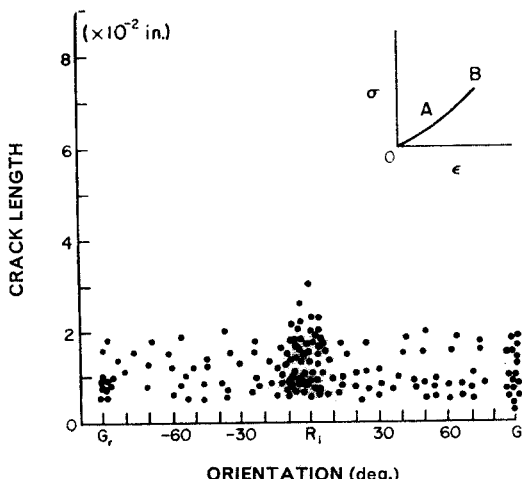


FIG. 26. Crack-length distribution for specimen loaded to an intermediate value.  $Ri$  is rift plane.  $Gr$  is grain plane. Cracks have not lengthened appreciably as shown by comparing this figure with Fig. 25. Cracks are concentrated around rift and grain planes.

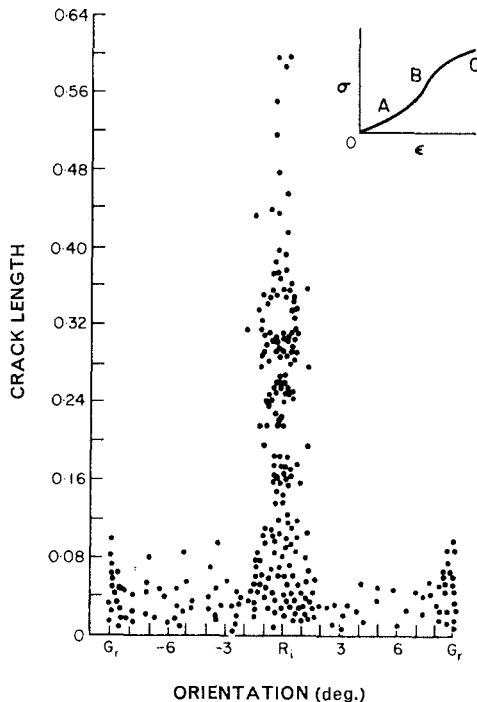


FIG. 27. Distribution of crack lengths relative to quarry directions in a specimen of granite subjected to high axial load. Specimen loaded parallel to rift ( $R_i$ ) and cracks markedly lengthened in that direction (compare with Fig. 25). Horizontal cracks, in plane of grain ( $G_r$ ), lengthened slightly. Boundary condition was *perfect confinement*.

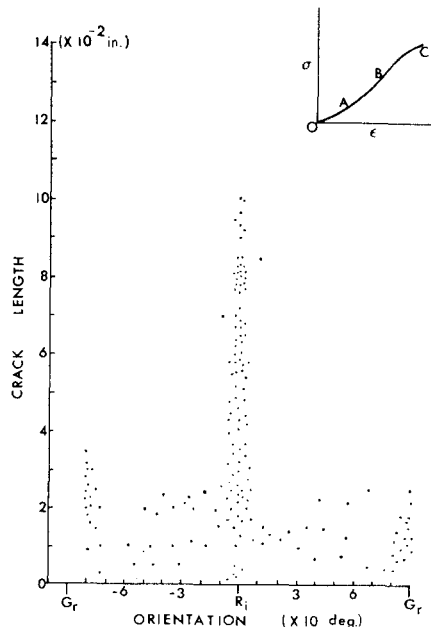


FIG. 28. Distribution of crack lengths relative to quarry directions in a specimen of granite subjected to high axial load and to *uniform loading*. Specimen loaded parallel to rift ( $R_i$ ) and cracks markedly lengthened in that direction (compare with Fig. 25). Horizontal cracks, in plane of grain ( $G_r$ ), lengthened slightly.

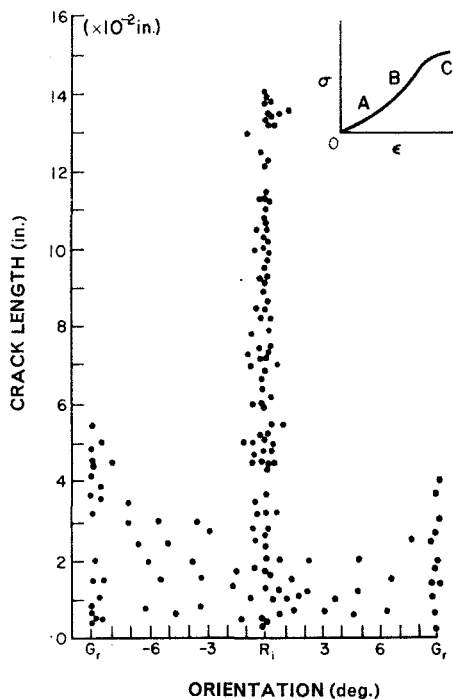


FIG. 29. Distribution of crack lengths relative to quarry direction in a specimen of granite subjected to high axial load and to *direct contact* end conditions. Note that scale in this figure is different from that in Figs 25-28. Specimen loaded parallel to rift ( $R_i$ ) and cracks lengthened markedly in that direction. Horizontal cracks also have lengthened markedly, as much as those parallel to the rift for uniform loading (Fig. 28).  
*Gr* is the grain quarry direction.

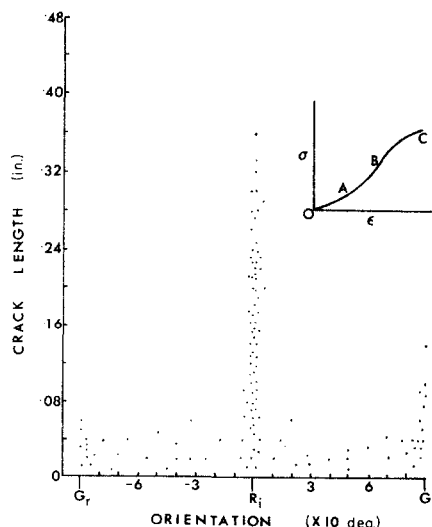


FIG. 30. Distribution of crack lengths relative to quarry directions in a specimen of granite subjected to high axial load and to *neoprene inserts* end conditions. Note that scale is different from that in Figs 25-28. Crack lengths have markedly increased in direction of rift ( $R_i$ ) and significantly increased in direction of grain ( $Gr$ ). Sample was loaded in direction of rift.

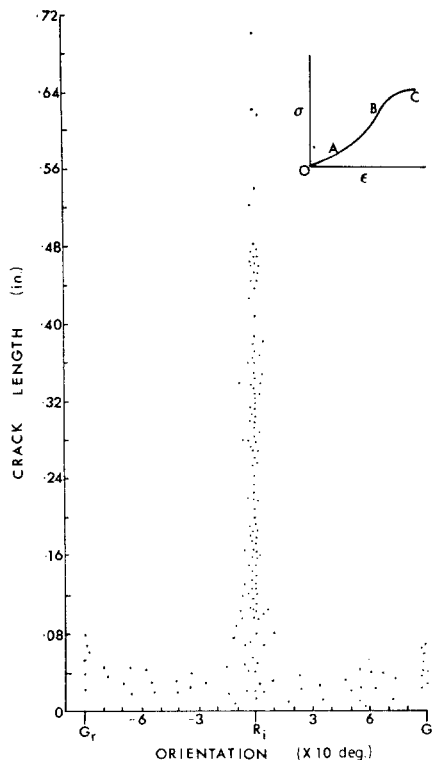


FIG. 31. Distribution of crack lengths relative to quarry directions in a specimen of granite subjected to high axial load and to *teflon inserts* end conditions. Crack lengths have greatly increased in direction of rift ( $R_i$ ), the loading direction, and significantly increased in direction of grain ( $G_r$ ), at right angles to loading direction.

The cracks parallel to the rift markedly lengthened; their lengths ranged from 0.002 to 0.14 in. Crack lengths in other orientations varied from 0.001 to 0.005 in. Horizontal cracks, parallel to the grain, lengthened slightly.

Figure 28 shows crack-length distributions for a specimen under uniform loading. About 74 per cent of the 716 cracks measured were within  $10^\circ$  of the rift plane; their lengths ranged from 0.001 to 0.10 in. Those with other orientations ranged from 0.002 to 0.035 in.

For a specimen subjected to direct contact (Fig. 29), 67 per cent of the 533 cracks measured were within  $20^\circ$  of the rift plane and ranged in length from 0.016 to 0.62 in. Crack lengths in other orientations ranged from 0.006 to 0.104 in.

For a specimen with end conditions of neoprene inserts (Fig. 30), 79 per cent of the 642 measured cracks were within  $10^\circ$  of the rift plane and had lengths ranging from 0.012 to 0.36 in. Crack lengths in other orientations ranged from 0.008 to 0.14 in.

Figure 31 shows that, for end conditions of teflon inserts, 81 per cent of the cracks were within  $10^\circ$  of rift plane. Their lengths ranged from 0.008 to 0.70 in. Crack lengths in other orientations varied from 0.004 to 0.08 in.

#### 4.4 Theoretical analysis of the location of intense crack growth in specimens

We have shown that, regardless of boundary conditions, most of the cracks that lengthened markedly in Chelmsford granite were parallel to the rift plane, which, in turn,

was parallel to the direction of loading. Cracks with other orientations did not lengthen appreciably. The reason for this phenomenon has been explained in a different context by BRACE and BOMBOLAKIS [17] and HOEK [18]. By forming cracks in glass plates and then subjecting the plates to uniaxial compression, Brace and Bombolakis found that the most severely stressed crack is inclined at about  $30^\circ$  to the axis of compression. Such cracks, when either isolated or placed in an array, grow along a curved path which becomes parallel to the direction of compression. HOEK [18] reached the same conclusion.

BIENIAWSKI [29] showed that, if similar glass plates containing very thin cracks are subjected to uniaxial compression, the cracks close and many tiny branching cracks grow along boundaries of the closed cracks, as a result of frictional sliding. The tiny cracks grow along closed cracks that are inclined about  $30^\circ$  to the direction of loading and all the tiny cracks tend to become parallel to the direction of compression.

The initiation of cracks is usually explained by the Griffith theory, which assumes that failure takes place where the maximum tensile stress along a crack reaches the theoretical strength of the material. Griffith [14, 15] derived his criterion of failure for two-dimensional stresses by studying, in detail, the variation of the circumferential stress,  $\sigma$ , along the surface of a flat elliptical crack of semi-axes,

$$a = c \cosh \xi_0, \quad b = c \sinh \xi_0.$$

Here,  $\xi_0$  is a constant in elliptical coordinates,  $a$  and  $b$  are the major and minor axes of the crack, and  $c$  is the focal length. Under such conditions, the maximum tensile stress along the surface of the critical crack is

$$\sigma = - \frac{(\sigma_1 - \sigma_3)^2}{4(\sigma_1 + \sigma_3) \xi_0}. \quad (1)$$

The maximum tensile stress,  $\sigma$ , does not occur at the tip, but close to the tip of the crack [16].

If friction between the surfaces of closed cracks is taken into account, equation (1) becomes [43]

$$\sigma = - \frac{1}{4\xi_0} [(\sigma_1 - \sigma_3)(1 + \mu)^{\frac{1}{2}} - \mu(\sigma_1 + \sigma_3)] \quad (2)$$

where  $\mu$  is the coefficient of internal friction.

PENG [25, 26] has shown that the magnitudes and orientations of the principal stresses do not differ significantly from those of the axial, radial and circumferential stresses. Therefore, in two dimensions, we can take axial stress as the maximum compressive stress and radial stress as minimum compressive stress. Also, according to equations (1) and (2), for constant values of crack size: (i) the larger the maximum compression,  $\sigma_1$ , the larger the tensile stress,  $\sigma$ , developed near the crack tip, and (ii) if the minimum stress,  $\sigma_3$ , is tensile, then, the larger its magnitude, the larger the tensile stress,  $\sigma$ , developed near the crack tip. Presumably, cracks subjected to the highest tensile stress can be expected to initiate and propagate earlier than other cracks.

As is shown in Fig. 12, radial and circumferential stresses are compressive in certain parts of a specimen and tensile in other parts. Further, axial stresses are highly concentrated in corners of specimens for boundary conditions of perfect confinement and direct contact and in the center of the end of the specimen for boundary conditions of neoprene inserts (Fig. 12). The areas of high axial compressive stresses and areas of relatively high tensile stresses

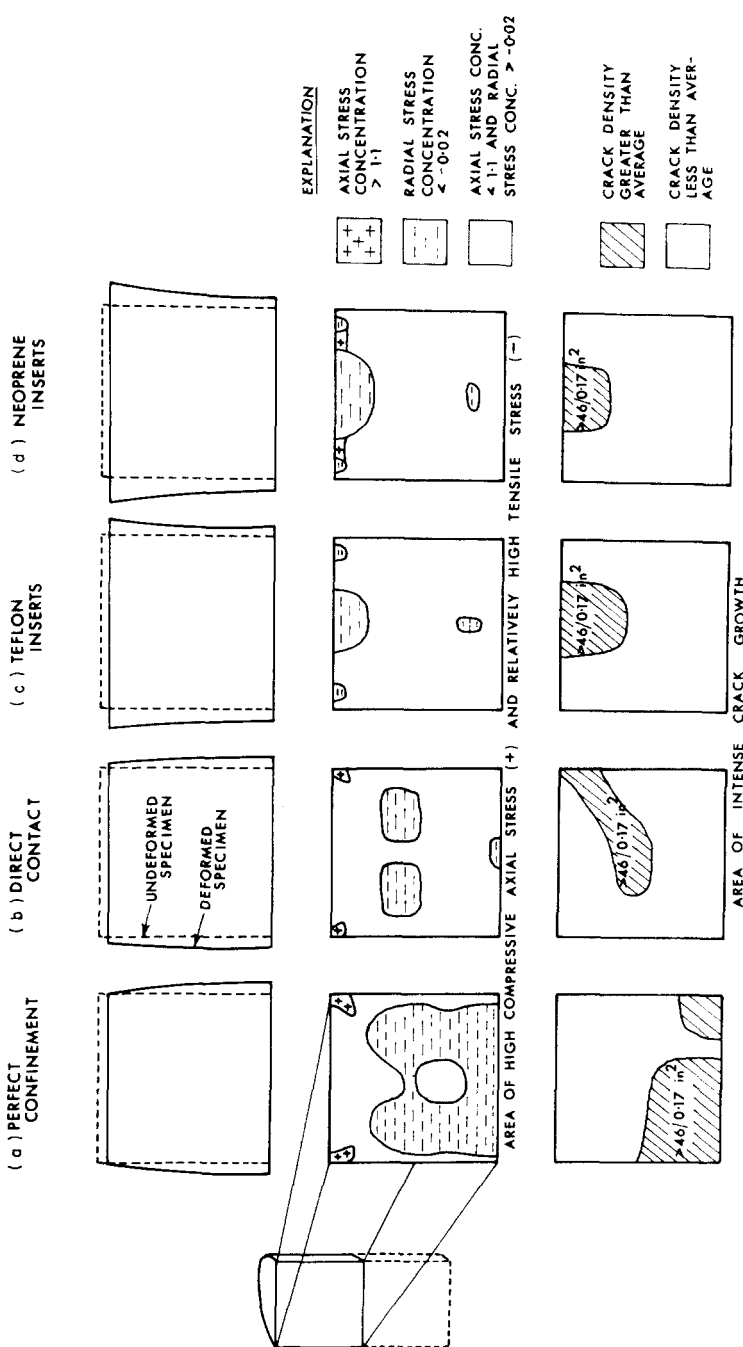


FIG. 32. Comparison of areas of intense crack growth with areas of relatively high concentration of tensile radial stress in upper halves of specimens of Chelmsford granite. First row of figures shows deformed shapes of upper halves of specimens. Middle row shows areas of relatively high stress concentration. Bottom row shows areas of intense crack growth, simplified from Fig. 20.

should be the areas of most intense crack growth in specimens. The second row in Fig. 32 shows areas where axial stress concentration is greater than  $+1.1$  and areas where radial or circumferential stress concentrations are more tensile than  $-0.02$ . Thus, the areas shown with negative signs or with plus signs in Fig. 32 are areas where we would expect cracks to propagate the most as a specimen is loaded.

The third row of diagrams in Fig. 32 shows areas where crack densities are greater than or less than 46 cracks per area of  $0.17 \text{ in}^2$ , which is about the average crack density for boundary condition of uniform loading (Fig. 15). The diagrams in Fig. 32 are simplifications of the contour maps of crack density shown in Fig. 20.

The correlation between the areas of intense cracking and the areas of relatively high tensile radial stresses is striking. The theoretical stress distribution indicates most intense crack growth in the middle of specimens subjected to perfect confinement and that is where the most intense cracking is observed. For direct contact, in contrast, most intense crack growth should be at midheight of the upper half of a specimen [Fig. 32(b)] and that is where the crack density is highest. The actual sizes of areas of intense crack growth shown in Figs 32(a) and 32(b) are not the same as the areas of relatively high tension. However, the positions of intense crack growth are as predicted by theory. Figures 32(c) and 32(d) also show strong correlations between theory and experiment.

We feel that it is reasonable to conclude that the combination of the theoretical solution for the stresses around an elliptic hole in an elastic plate, which is fundamental to Griffith's theory, and PENG's [25, 26] theoretical solution for stresses within elastic cylindrical specimens subjected to various boundary conditions, predicts the positions of intense crack growth in specimens of Chelmsford granite.

## 5. ULTIMATE COMPRESSIVE STRENGTHS AND FRACTURE CRITERIA OF CHELMSFORD GRANITE

In the preceding section we studied propagation and growth of cracks within specimens of Chelmsford granite subjected to uniaxial and triaxial loading. The crack patterns developed immediately before gross failure of specimens are different for different boundary conditions. Now we will examine the modes of gross fracture and the ultimate compressive strengths for the various boundary conditions and discuss possible fracture criteria to account for them.

### 5.1 *Ultimate compressive strengths of Chelmsford granite*

Ultimate strength can be defined as  $P/A$ , where  $P$  is the maximum axial load that a specimen can sustain and  $A$  is the cross-sectional area of the specimen.

The ultimate strength of Chelmsford granite varies with imposed end-boundary conditions. For example, Fig. 33 shows that the ultimate compressive strengths of cylindrical specimens, with diameters of  $1\frac{1}{4}$  in. and with long axes perpendicular to the rift plane ( $R$ -specimens), are 29,500 psi for perfect confinement; 26,400 psi for direct contact; 25,300 psi for uniform loading; 20,300 psi for teflon inserts, and 15,400 psi for neoprene inserts.

For specimens where long axes are perpendicular to the hardway plane ( $H$ -specimens), the ultimate strengths are 28,700 psi for perfect confinement; 24,700 psi for direct contact; 24,600 psi for uniform loading; 18,400 psi for teflon inserts, and 15,100 psi for neoprene inserts. Figure 33 shows the average ultimate strengths for specimens the long axes of which are perpendicular to the grain plane ( $G$ -specimens). They are 26,500 psi for perfect confine-

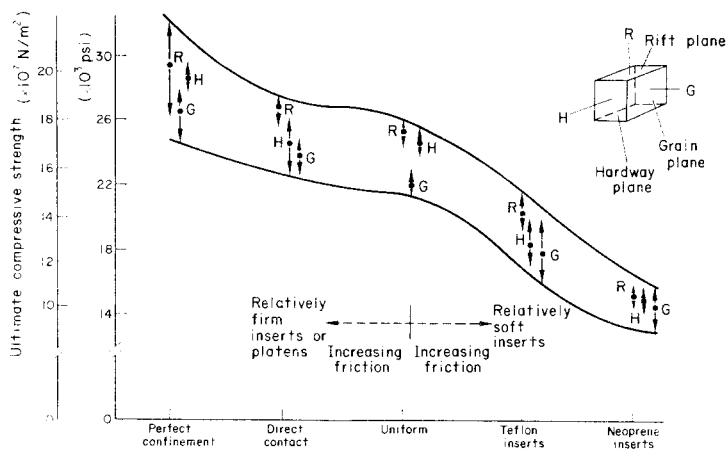


FIG. 33. Ultimate compressive strengths for specimens of Chelmsford granite as functions of specimen orientation and end-boundary condition.

ment; 23,800 psi for direct contact; 22,000 psi for uniform loading; 16,900 psi for teflon inserts and 14,500 psi for neoprene inserts.

Thus, the ultimate strength of Chelmsford granite is not a constant, rather it varies with boundary conditions. The five boundary conditions are listed below in decreasing order of strengths attained: perfect confinement, direct contact, uniform loading, teflon inserts and neoprene inserts. The ratio of strengths between perfect confinement and neoprene inserts is on the order of two.

Ultimate strength of Chelmsford granite also varies with orientation of the specimen. Regardless of boundary condition, *R*-specimens are strongest, next comes *H*-specimens and *G*-specimens are weakest. The strength ratio between *G*-specimens and *R*-specimens ranges from 0.84 to 0.94, depending on boundary condition (Fig. 33).

PENG [25] has shown that the ultimate strengths of cylindrical specimens with  $1\frac{1}{4}$  in. and  $\frac{5}{8}$  in. diameters are nearly the same, regardless of boundary condition. He also showed that ultimate strengths of rectangular prisms are less than those of circular cylinders so that shape also significantly affects the ultimate strength of samples of Chelmsford granite.

As has been shown by other investigators, the ultimate compressive strength of rock is a function of confining pressure. Chelmsford granite is no exception, as is shown in Table 6. For end conditions of direct contact, the ultimate strength of Chelmsford granite ranges from about 26,400 psi for zero confining pressure to about 64,000 psi for a confining pressure of 10,000 psi. Mohr circles for Chelmsford granite are shown in Fig. 34, where each value of maximum compressive stress plotted is the average axial stress delivered to the specimen and where each value of the minimum (=intermediate) compression plotted is the confining pressure. The Mohr failure envelope appears to be nonlinear for confining pressures in excess of about 5000 psi (Fig. 34).

## 5.2 Fracture modes of Chelmsford granite

As we have shown, cracks in specimens subjected to end-boundary conditions of perfect confinement grow parallel to axes of specimens and are concentrated near midheight in

TABLE 6. ULTIMATE COMPRESSIVE STRENGTH AS A FUNCTION OF BOUNDARY CONDITIONS AND CONFINING PRESSURES FOR R-SPECIMENS

Confining pressure (psi)	Ultimate compressive strength (psi)			
	Perfect confinement	Direct contact	Teflon inserts	Neoprene inserts
0	29,500	26,400	20,300	15,400
1000	32,500	30,000	25,100	23,000
2000	35,900	35,000	31,700	29,700
3000	40,900	39,900	38,500	—
4000	—	44,700	—	—
5000	—	49,000	—	—
10000	—	64,000	—	—

specimens (Fig. 20). The longest cracks are near the outer edges (Fig. 27). Accordingly, the specimens fail first by flaking of pieces from their cylindrical surfaces, at midheight, causing them to become slender (Fig. 35). Failure becomes complete when the applied load is adequate to cause buckling of the slenderized specimen.

Under the end-boundary condition of direct contact, on the contrary, the cracks grow near the corners and in the center of the upper (and lower) half of a specimen (Fig. 20). The cracks grow parallel to the axis of the specimen (Fig. 29). A specimen fails by the formation of a cone at each end [Fig. 36(a)] or by the formation of a single fault, inclined to the axis of the specimen [Fig. 36(b)]. Combinations of these two failure modes can be recognized in many samples.

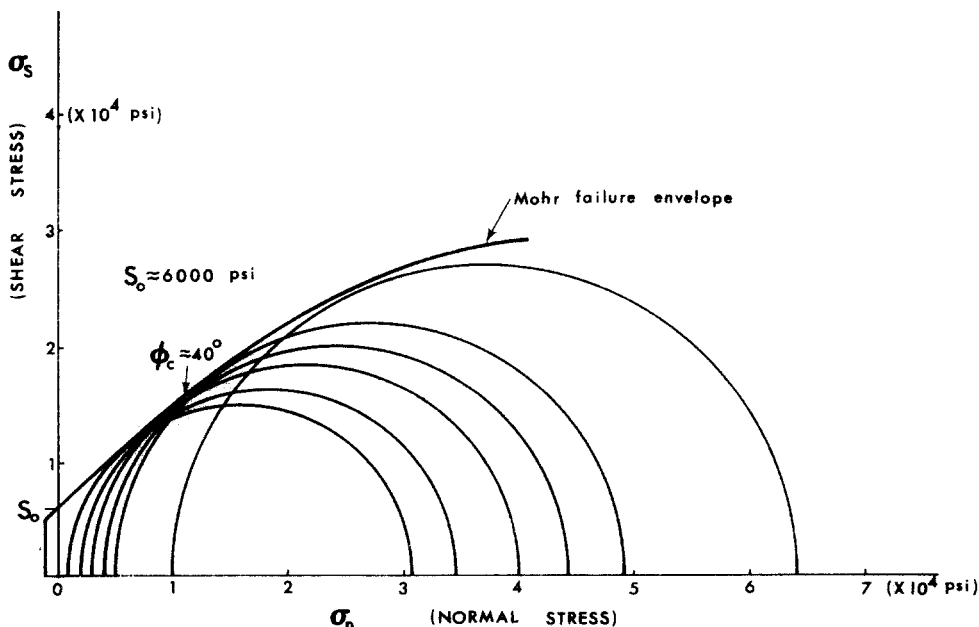


FIG. 34. Mohr circles for Chelmsford granite subjected to end condition of direct contact and various confining pressures.

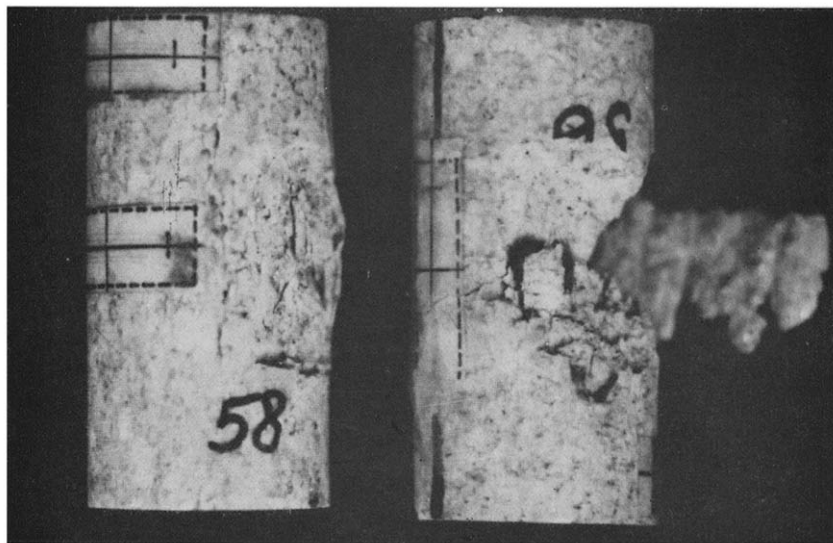


FIG. 35. Typical mode of failure of specimens of Chelmsford granite subjected to end condition approaching that of perfect confinement. Narrow hose clamps were placed around each end of specimen. Specimens first flaked at midheight and then the slenderized specimens buckled.

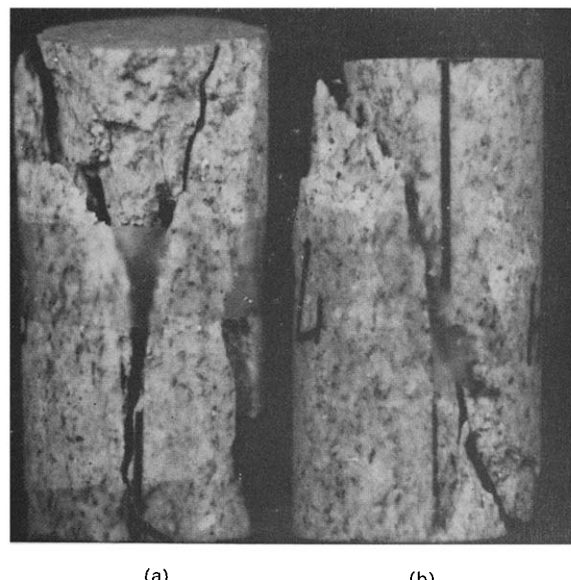


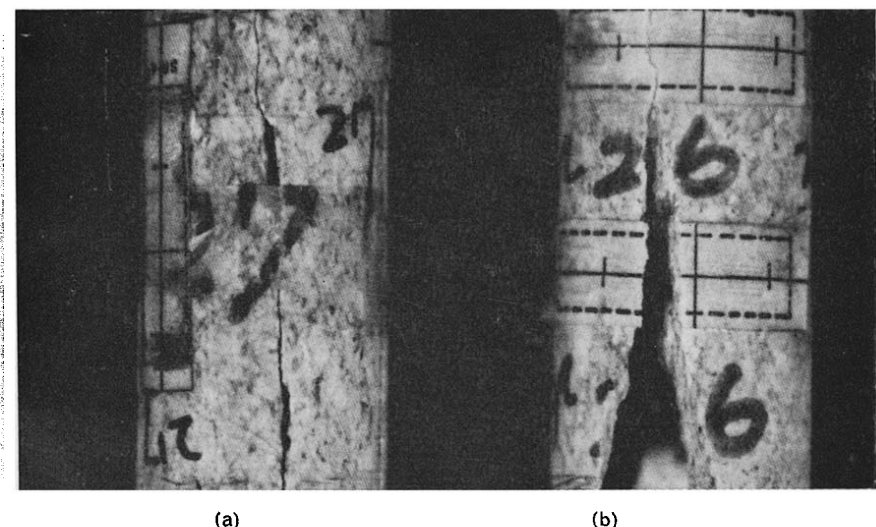
FIG. 36. Typical modes of faulting of specimens of Chelmsford granite which were placed in *direct contact* with the loading platens.



(a)

(b)

FIG. 37. Mode of fracture of specimens of Chelmsford granite subjected to end conditions of *uniform loading*.  
Samples typically split along one or more vertical fractures.



(a)

(b)

FIG. 38. Mode of failure of specimens of Chelmsford granite loaded uniaxially under end conditions of (a) *neoprene inserts* and (b) *teflon inserts*. Failure is by longitudinal splitting of specimens.

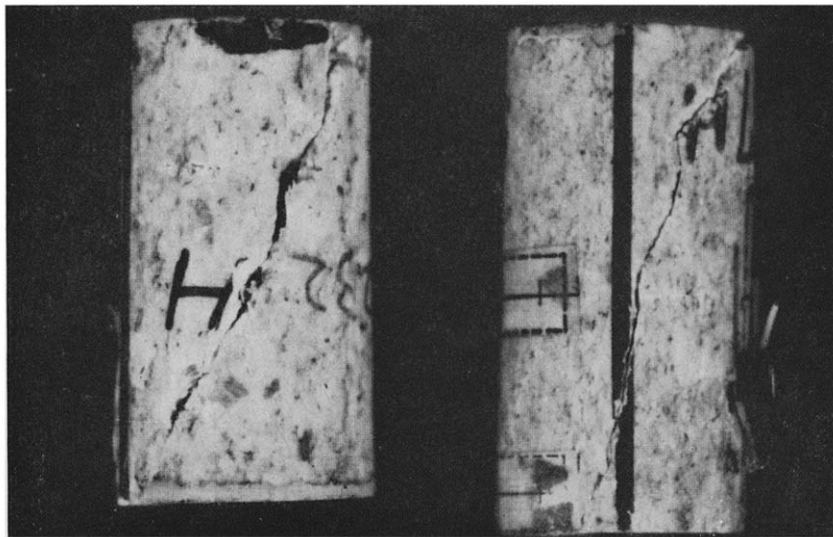


FIG. 39. Mode of failure of specimens of Chelmsford granite loaded triaxially under end conditions of (b) direct contact and (a) neoprene inserts. The failure mode for triaxial conditions seems to be independent of end-boundary conditions. Failure is generally by faulting.

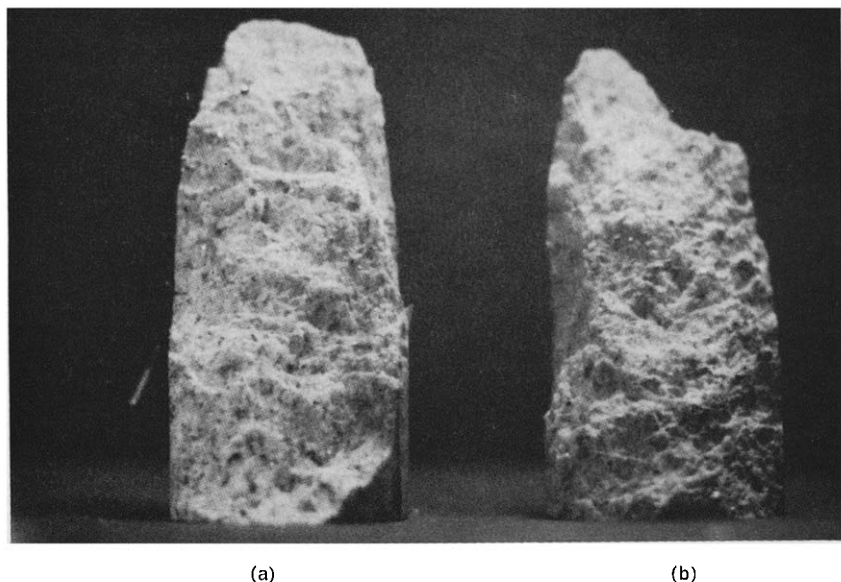


FIG. 40. Surfaces of faults within specimens of Chelmsford granite loaded (a) triaxially and (b) uniaxially under direct contact end conditions. Fault surface consists of many steps arranged as in a staircase. The surfaces of the steps are roughly perpendicular to the long axis, whereas the vertical risers are parallel to the long axis and are bounded by cracks parallel to the rift.

In samples subjected to uniform loading, cracks grow randomly in location, but they are oriented parallel to the axes of specimens (Figs 15 and 28). Specimens fail typically by longitudinal splitting (Fig. 37). The positions and the number of splits are variable, from sample to sample, as shown in Figs 37(a) and 37(b). Ultimate failure is by buckling of the split slabs of a specimen.

For end-boundary conditions of both neoprene inserts and teflon inserts, cracks grow preferentially parallel to the axes of the specimens (Figs 23, 24, 30 and 31) as for all other boundary conditions, but they are mostly located near the ends of specimens (Fig. 20). Specimens fail by longitudinal splitting (Fig. 38). Teflon inserts seem to promote the formation of a more irregular fracture plane than do neoprene inserts.

Specimens that have failed under triaxial loading typically fail along one or more planes inclined to long axes of specimens, regardless of end-boundary condition (Fig. 39).

### 5.3 *Splitting of cylindrical specimens*

Cylindrical specimens of Chelmsford granite fail by longitudinal splitting (Figs 37 and 38) if they are uniaxially loaded under conditions of uniform loading, teflon inserts or neoprene inserts. Specimens fail by flaking (Fig. 33) at midheight if they are subjected to perfect confinement; longitudinal splits through the entire specimen do not form in this case.

We were able to predict quite accurately the positions of intense crack growth in specimens by means of the theoretical solution for stresses and the basic concepts of Griffith's criterion of crack propagation. We can also explain qualitatively the differences in uniaxial compressive strength of samples subjected to end conditions of uniform loading, teflon inserts and neoprene inserts. The axial stress concentrations are maximum (1·2) for neoprene inserts, intermediate (1·1) for teflon inserts and minimum (1·0) for uniform loading. The radial stress concentrations are significantly different also (Fig. 12); they are essentially zero for uniform loading, -0·04 for teflon inserts and -0·06 for neoprene inserts. Thus, the relative values of compressive axial and tensile radial stresses developed within specimens correlates with the relative values of uniaxial compressive strengths for these boundary conditions (Fig. 33).

PENG [25] has applied the concept of fracture toughness, described in Section 2, to predict the ultimate compressive strengths of samples subjected to uniform loading, teflon inserts and neoprene inserts in terms of known values of fracture toughness and crack lengths. The concept of fracture toughness has not been clearly developed for conditions imposed by uniaxial testing, however, so that we will not apply it here.

Failure by flaking and ultimate collapse of the resulting slenderized specimen, such as we see in samples subjected to perfect confinement, cannot be predicted by any theory known to us. The positions of intense crack growth can be predicted, as we have shown, but the high ultimate strengths of specimens subjected to perfect confinement cannot. They can be understood, however, in terms of the boundary conditions imposed on the specimens. Growth of long, longitudinal cracks was inhibited near the ends of specimens subjected to perfect confinement because this end condition was achieved by tightly fixing a narrow hose clamp around each end of the specimen. Also, cracking near the corners was inhibited by the clamps so that faults, such as those shown in Fig. 36, could not form readily either. Apparently, therefore, the high compressive strengths of samples subjected to perfect confinement was caused by high stress intensities required to cause specimens to flake at mid-height and, ultimately, to cause buckling.

### 5.4 Criterion of faulting of cylindrical specimens of Chelmsford granite

*Characteristics of fault surfaces.* Direct contact between the ends of the specimen and the platens of the loading machine is the end-boundary condition most commonly used in laboratory strength-testing. If end friction is low, as shown in earlier pages, the specimens tend to fail along planes, or faults, inclined to long axes of specimens (Fig. 36). Specimens subjected to triaxial loading fail the same way, regardless of end-boundary conditions (Fig. 39). On the other hand, if end friction is high in uniaxial loading, the specimens tend to fail along roughly cone-shaped faults, the bases of the cones originating at the sample ends [Fig. 36(a)].

A feature of particular interest is the detailed shape of fault surfaces in specimens. The shape of typical fault surfaces is shown in Fig. 40; the surface is far from a simple, smooth plane. Instead, it consists of many tiny steps, arranged as in a staircase. The surfaces of the steps are roughly perpendicular to the long axis of the specimen, that is, to the direction of applied load, whereas the risers are parallel to the long axis. The vertical risers, presumably, are surfaces of cracks which have propagated longitudinally within the specimen; we have shown, repeatedly, that longitudinal cracks in cylindrical specimens of Chelmsford granite grow in length more than cracks with other orientations (Figs 27–31). The horizontal steps, presumably, are partly cracks that propagated as the specimen was loaded and are partly cracks that formed at the time the gross failure plane developed.

Any failure criterion adopted for the formation of faults in specimens of Chelmsford granite must account for these features of the fault surfaces. The Coulomb and Griffith theories do not account for these features.

We suggest that it is reasonable to assume that, at the moment of gross failure, the areas between the parallel cracks behaved as tiny columns or beams of rectangular cross section. Then lateral deflection and failure of the tiny columns or beams, aligned along paths of faults in specimens of Chelmsford granite, could account for development of the faults. The process is shown schematically in Fig. 41, both for a single fault plane and for cone-shaped fault planes.

We will develop a tentative theory for the deflection of the tiny columns or beams, assuming that they are cantilever beams with one end or both ends built in and consider buckling to be the cause of the 'staircase' on the fault surfaces. Inspection of the deformed specimens of Chelmsford granite indicates that the tiny columns or beams have length-to-width ratios on the order of ten so that the tiny specimens should behave mechanically as beams rather than as short columns [44].

We fully realize that there are serious conceptual difficulties facing the use of beam theory to predict buckling of the small pieces of granite bounded by the vertical, longitudinal cracks. One problem is that the dimensions of the small beams are of the order of the dimensions of the mineral grains in Chelmsford granite. The mineral grains are definitely anisotropic and contain many flaws. Another problem is that the mechanisms of failure of the tiny beams are unknown; perhaps they fail because of stress concentration at crack tips rather than because of fiber stresses along the surfaces of columns, as we will assume. Because of these and other difficulties, the theory that we are proposing should be considered to be tentative. We are quite sure, however, that specimens of Chelmsford granite actually do fault by a complicated process of buckling on a small scale.

*Beam-buckling theory of faulting.* Figure 41(a) shows part of an idealized crack pattern developed in a specimen of Chelmsford granite loaded under end conditions of low-friction, direct contact. We have shown that, at the time immediately before failure, most cracks are

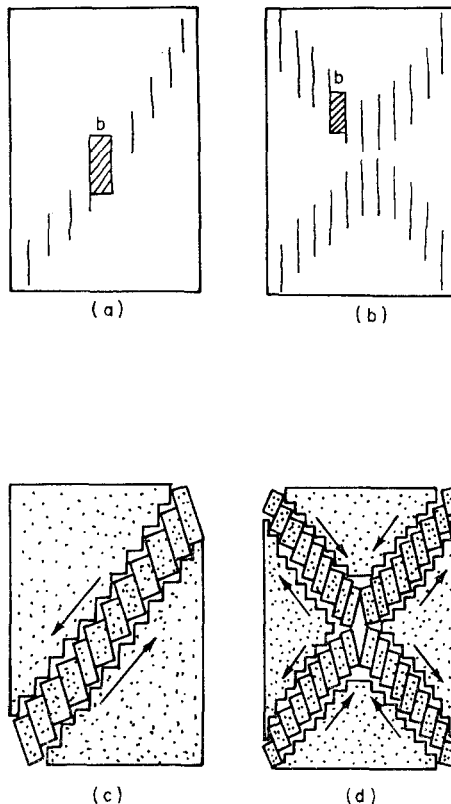


FIG. 41. Idealized concept of development of faults in cylindrical specimens. Cracks propagate parallel to the specimen axis. 'Simple shear' fault plane, in (c) develops by bending and ultimate fracturing of small columns or beams which are bounded by vertical cracks. Cone-in-cone or 'pure shear' fault planes, in (d) form if specimen ends do not move laterally relative to each other during failure of the specimen.

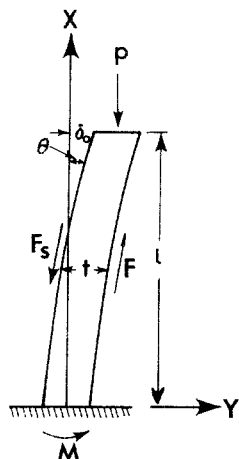
oriented roughly parallel to the long axes of the specimens. Detailed examination of faults in granite specimens suggests that the failure of tiny beams of granite between cracks accounts for the formation of the faults [Figs 41(c) and 41(d)].

Each small beam, such as *b* in Fig. 41(a), will be represented by a cantilever beam with a built-in end [Fig. 42(a)]. The cantilever beam will be assumed to be initially inclined with respect to the axis of the specimen. Forces and moments acting on the beam are: *P*, axial load; *F<sub>s</sub>*, shear force; and *M*, bending moment. The shear force is due to frictional interaction between adjacent beams and is a function of confining pressure and friction among adjacent beams. As is shown in Fig. 42(a), *l* is the length and *t* is the width of a beam.

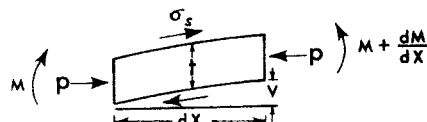
If the fixed end of the cantilever is the origin of coordinates, the beam is initially deflected according to the expression [20]

$$v_0 = \delta_0 \left[ 1 - \cos \left( \frac{\pi x}{2l} \right) \right] \quad (3)$$

where  $\delta_0$  is the deflection of the free end ( $x = l$ ).



(a)



(b)

FIG. 42. Single beam within specimen isolated for analysis of equilibrium.

Figure 42(b) is an infinitesimal element cut from the beam shown in Fig. 42(a). For equilibrium, the summation of moments about any point must vanish, so that

$$M - M - \frac{dM}{dx} \delta x - P \frac{dv}{dx} + \sigma_s b t \delta x = 0 \quad (4)$$

where  $\sigma_s$  is the shear stress ( $\sigma_F \tan \theta$ ) among beams and  $v$  is the *total* deflection of the beam. That is,  $v$  is the initial deflection,  $v_0$ , plus the additional deflection,  $v_1$ , caused by the axial load,  $P$ .

Replacing  $v$  by  $v_1 + v_0$  in equation (4)

$$\frac{dM}{dx} + P \left( \frac{dv_1}{dx} + \frac{dv_0}{dx} \right) - \sigma_s b t = 0. \quad (5)$$

Integrating equation (5) with respect to  $x$

$$M + P(v_1 + v_0) - \sigma_s b t x = c_1 \quad (6)$$

where  $c_1$  is an arbitrary constant.

Substituting  $M$  by  $-EI(d^2v_1)/(dx^2)$  in equation (6) and rearranging [20, 44]:

$$-EI \frac{d^2v_1}{dx^2} + Pv_1 = c_1 + \sigma_s btx - Pv_0. \quad (7)$$

The homogeneous solution of equation (7) is

$$(v_1)_{\text{homo}} = c_2 \sin \alpha x + c_3 \cos \alpha x \quad (8)$$

where  $\alpha^2 = P/EI$ .

The particular solution of equation (7) assumes the form

$$(v_1)_{\text{part.}} = A + Bx + C \cos \left( \frac{\pi x}{2l} \right). \quad (9)$$

Substituting equation (9) into equation (7), and equating corresponding terms

$$C = \frac{\delta_0}{1 - \frac{P_1}{P}} \quad (10)$$

$$B = \frac{\sigma_s bt}{P} \quad (11)$$

where

$$P_1 = EI \left( \frac{\pi}{2l} \right)^2 \quad \text{and} \quad A = \frac{c_1}{P} - \delta_0. \quad (12)$$

Therefore, the general solution of equation (7) is

$$v_1 = c_2 \sin(\alpha x) + c_3 \cos(\alpha x) + \left( \frac{c_1}{P} - \delta_0 \right) + \frac{\sigma_s bt}{P} x + \frac{\delta_0}{1 - \frac{P_1}{P}} \cos \left( \frac{\pi x}{2l} \right). \quad (13)$$

The coefficients  $c_2$  and  $c_3$  in equation (13) can be eliminated by means of the following boundary conditions:

$$\text{at } x = 0, v = 0, \frac{dv_1}{dx} = 0 \quad (14)$$

$$\text{at } x = l, \frac{d^2v_1}{dx^2} = 0. \quad (15)$$

Differentiating equation (13)

$$\frac{dv_1}{dx} = c_2 \alpha \cos(\alpha x) - c_3 \alpha \sin(\alpha x) + \frac{\sigma_s bt}{P} - \frac{\delta_0(\pi/2l)}{1 - P_1/P} \sin \left( \frac{\pi x}{2l} \right). \quad (16)$$

Differentiating equation (16)

$$\frac{d^2v_1}{dx^2} = -c_2 \alpha^2 \sin(\alpha x) - c_3 \alpha^2 \cos(\alpha x) - \frac{\delta_0(\pi/2l)^2}{1 - P_1/P} \cos \left( \frac{\pi x}{2l} \right). \quad (17)$$

Substituting equation (17) into equation (15)

$$c_2 = -c_3 \cotan(\alpha l). \quad (18)$$

Substituting equation (18) into equations (14) and (16)

$$c_2 = -\frac{\sigma_s b t}{a P}. \quad (19)$$

Thus, from equations (18) and (19)

$$c_3 = \frac{\sigma_s b t}{a P} \tan\left(\frac{\pi}{2} \sqrt{\frac{P}{P_1}}\right). \quad (20)$$

The fiber strain at the origin is

$$\epsilon_f = \frac{t}{2} \frac{d^2 v_1}{dx^2} \quad (21)$$

so that, at  $x = 0$

$$\epsilon_f = -\frac{\sigma_s b t^2}{2 P} \alpha - \frac{\delta_0 (\pi/2l)^2 t/2}{1 - P_1/P} \quad (22)$$

or

$$\epsilon_f = \frac{\sigma_s b t^2 \sqrt{(P/EI)}}{2 P} - \frac{(\delta_0/l) (t/l) \pi/8}{1 - P_1/P} \quad (23)$$

where  $P_1 = EI(\pi/2l)^2$  is defined as the critical load of a beam. It is equivalent to the critical Euler load for an unconfined beam of length  $2l$  (for example see JOHNSON [20] and TIMOSHENKO *et al.* [44, 45]).

Equation (23) can be rearranged as

$$\epsilon_f = \left(\frac{t}{l}\right) \left(\frac{\pi}{4}\right) \left[ \left(\frac{\delta_0}{2l}\right) \frac{1}{(\sigma_c/\sigma_a - 1)} - \frac{\sigma_s}{\sigma_a} \sqrt{\frac{\sigma_c}{\sigma_a}} \right] \quad (24)$$

where

$$\sigma_a = \frac{P}{bt}, \quad \text{and} \quad \sigma_c = \frac{Et^2}{12} \left(\frac{\pi}{2l}\right)^2.$$

If we take the product  $t^2/l\delta_0 = 100$ , and plot the axial stress,  $\sigma_a/\sigma_c$ , with respect to  $\epsilon_f$ , the fiber strain, equation (24) can be expressed graphically as in Fig. 43. The graphs show that the relation between average axial stress and fiber strain at the fixed end of a beam is non-linear, especially for low values of shear stress, that is, for low values of confining pressure. Also, under constant axial stress the larger the shear stress, the smaller the fiber strain. Finally, the larger the shear stress (confining pressure), the larger the axial stress required to initiate bending.

Let us assume that the beams fail when the fiber strain,  $\epsilon_f$ , reaches a certain value characteristic of the material. Then, a relationship between axial stress and shear stress can be plotted as shown in Fig. 44(a). According to that figure, the axial stress required for failure increases sharply with increasing shear stress for low values (less than  $10^{-3}$ ) of the critical fiber strain. The curve flattens as  $\epsilon_f$  increases and becomes essentially horizontal

if  $\epsilon_f$  is larger than  $10^{-1}$ . Figure 44(b) is a similar plot of equation (24), except  $l^2/\delta_0 t = 1000$ , instead of 100 and the horizontal scale has been expanded by a factor of ten.

The effect of different initial inclinations of cracks within specimens is shown in Fig. 45, where  $\delta_0/l$  is the inclination of the cracks from the vertical. It shows that the axial stress required for faulting increases rapidly with shear stress if initial deflection,  $\delta_0$ , of the beams is small. The curve becomes gentler as initial deflection increases. Therefore, the smaller the

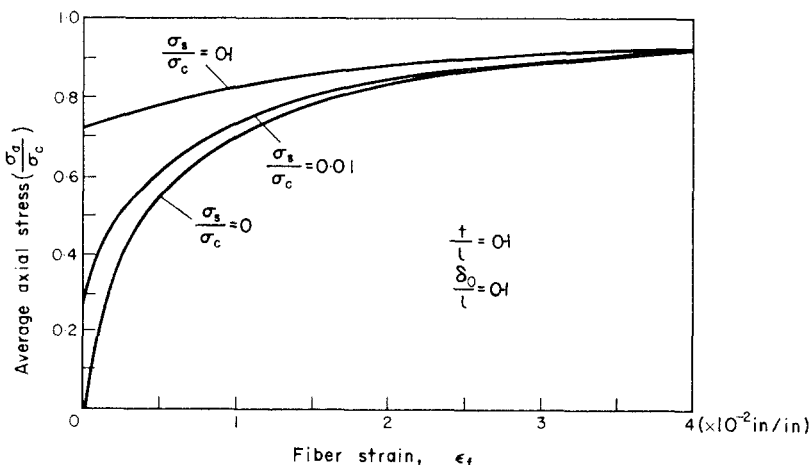


FIG. 43. Relation between average axial stress acting on specimen and maximum fiber strain of small beams within specimen for various values of shear stress among beams. The shear stress is proportional to the confining pressure acting on the specimen. As the shear stress or confining pressure increases, the axial stress required for deformation of the small beams approaches the critical, Euler axial stress,  $\sigma_c$ .

initial tilts of the cracks, the more marked is the effect of confining pressure on the average axial stress required for faulting. The initial deflection ratio,  $\delta_0/l$ , is the sine of the angle of inclination of the beams so that a value of  $\delta_0/l = 0.1$  corresponds with an angle of inclination of  $\theta = 6^\circ$  and a value of  $\delta_0/l = 0.01$  corresponds with an angle  $\theta = 0.5^\circ$ .

The experimental data for the ultimate strengths of specimens of Chelmsford granite, as a function of confining pressure, have been plotted in Fig. 46. The data are for end-boundary conditions of direct contact (Table 6). The data points have been fitted to a theoretical relation between average axial stress and confining pressure by arbitrarily selecting the following constants:

$$l/t = 10$$

$$l/\delta_0 = 10$$

and

$$\phi_b = 45^\circ \text{ (friction among beams)}$$

and by estimating the value of  $\delta_c = 95,000$  psi, which causes the value of uniaxial compressive strength to superimpose on the curve for a critical fiber strain of  $10^{-4}$  in Fig. 46.

Clearly, the data can be made to fit closely one or more of the theoretical curves derived from our beam-buckling theory. We realize, of course, that this close fit does not necessarily indicate that the theory is acceptable for describing the ultimate strengths of Chelmsford

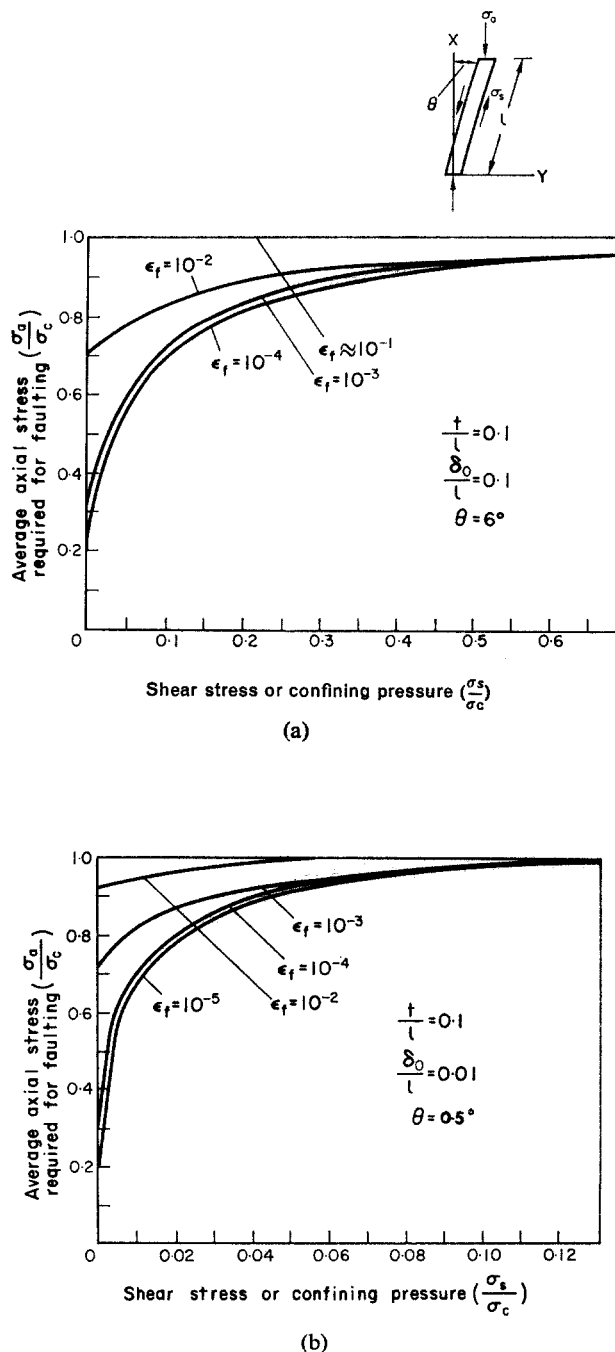


FIG. 44. Relation between average axial stress required for faulting and shear stress or confining pressure acting across cracks for several values of critical fiber strain. (a) Cracks initially tilted 6° from vertical. (b) Cracks initially tilted 0.5° from vertical.

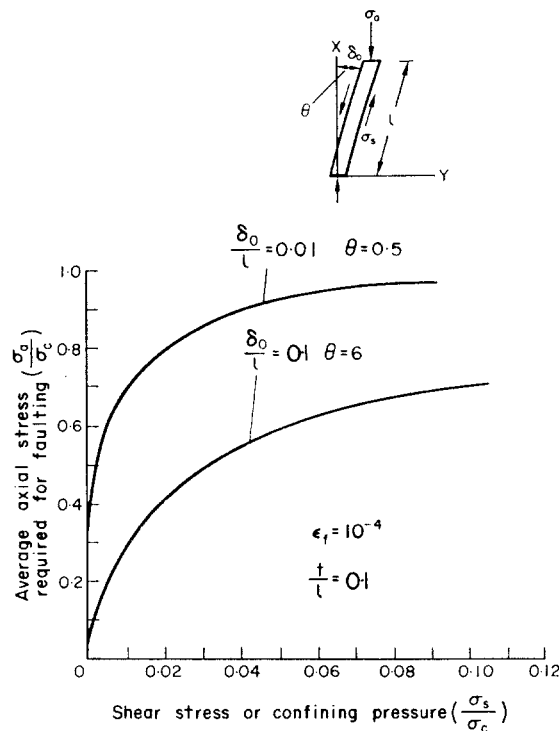


FIG. 45. Effect of initial tilt of cracks from vertical on relation between average axial stress required for faulting and shear stress or continuing pressure acting across cracks.

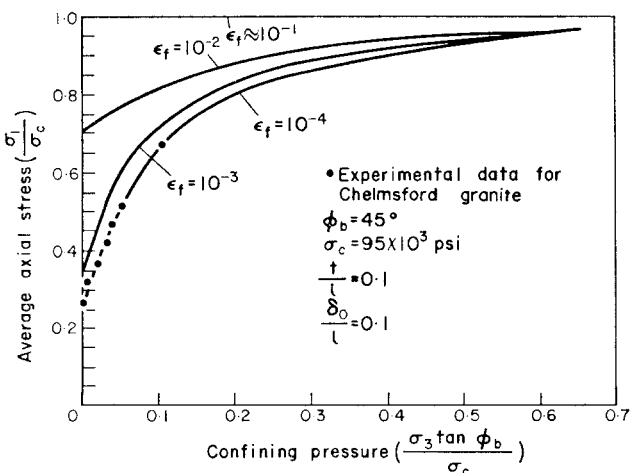


FIG. 46. Comparison of experimental data of compressive strengths of Chelmsford granite under end conditions of direct contact and various confining pressures, with theoretical relations predicted by beam-buckling theory of faulting. Friction angle across cracks assumed to be  $45^\circ$ .

granite. The close fit merely indicates that we need not reject our theory at this time. Further experimentation and analysis is required to evaluate the theory.

We have compared our experimental results with theoretical relations between confining pressure and ultimate strengths predicted by the Coulomb and the modified Griffith theories. According to the Coulomb theory [16]

$$\sigma_1[(\mu^2 + 1)^{\frac{1}{2}} - \mu] - \sigma_3[(\mu^2 + 1)^{\frac{1}{2}} + \mu] = 2S_0$$

where  $\mu = \tan \phi_c$  is the coefficient of Coulomb friction and  $S_0$  is the shear-stress intercept of the failure envelope on the Mohr diagram (Fig. 34). This equation predicts the upper, solid straight line in Fig. 47. According to the modified Griffith theory [16]

$$\sigma_1[(\mu^2 + 1)^{\frac{1}{2}} - \mu] - \sigma_3[(\mu^2 + 1)^{\frac{1}{2}} + \mu] = 4T_0$$

for the conditions of interest here. In this equation,  $T_0$  is the tensile strength of the material, and  $\mu = \tan \phi_g$  is the coefficient of friction acting across closed Griffith cracks. This equation is plotted as the lower straight line in Fig. 47.

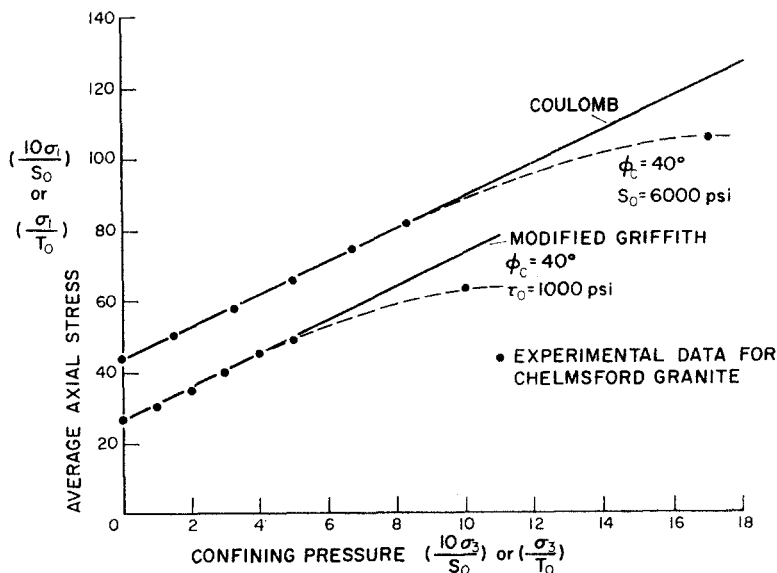


FIG. 47. Comparison of experimental data of compressive strengths of Chelmsford granite for various confining pressures with theoretical relations predicted by Coulomb theory and modified Griffith theory.

As indicated by JAEGER and COOK [16], the Coulomb and modified Griffith theories are essentially identical; they both predict a linear relation between ultimate compressive strength and confining pressure.

The theoretical relationships closely fit the experimental data for Chelmsford granite for confining pressures between zero and 5000 psi (Fig. 47). For a confining pressure of 10,000 psi, however, the theoretical strengths are considerably higher than the strength actually determined experimentally. Thus, both theories would be rejected for Chelmsford granite, assuming that the experimental results are adequate to define the actual relationship for the granite. The beam-buckling theory seems to be the best of the three theories, according to our experiments, for describing the ultimate compressive strength of Chelmsford granite.

*Comments on applicability of Coulomb's theory to faulting of rock.* As we indicated in the Introduction, we have serious doubts about the common use of Coulomb's theory to describe faulting of brittle rock. We maintain these doubts. However, we can imagine at least two possible processes of rock deformation that would provide a sound basis for using Coulomb's theory or some other theory of plasticity to describe faulting of rock. One process is plastic deformation of crystals within a rock. Plastic deformation might be operative at high confining pressures in rocks containing minerals such as feldspar and at lower confining pressure in rocks containing minerals such as calcite.

The other process involves crack growth. We can clearly imagine the situation where a brittle rock becomes essentially a granular solid as a result of initiation and propagation of cracks during loading of the rock [20]. The propagation of cracks in Chelmsford granite leads to a peculiar type of granular solid in which many of the 'granules' are shaped much as beams or rods. If, however, the 'granules' were more nearly equidimensional, the rock would behave much as a highly compact sand in which the 'granules' fit together as pieces of a three-dimensional jig-saw puzzle. Such a material could, indeed, behave mechanically as a granular solid. Perhaps the behavior of such a material could be described adequately in terms of Coulomb's theory. This remains to be demonstrated, however.

*Acknowledgments*—During the course of our investigation we have become indebted to many people, especially to DAVID POLLARD, Department of Geology, University of Rochester, New York, and KAARE HÖEG, Department of Civil Engineering, Stanford University, who read an early form of the manuscript and offered numerous helpful suggestions. We thank ATTILA KILINC, University of Cincinnati, Ohio, for reviewing the final manuscript. The senior author would like to thank STEVEN CHI and JOHN COGAN, fellow students at Stanford, for many hours of searching discussion about fracture mechanics. The research was generously supported with financial assistance from ARPA, through the Center for Materials Research, and from the Department of Mineral Engineering, Stanford University. We are grateful to ANDREW FLETCHER, H. E. Fletcher Co., North Chelmsford, Mass., for supplying the oriented blocks of granite used for the experiments.

## REFERENCES

1. BRODE H. L. Rock Mechanics Considerations in the Design of Underground Protective Structures, in *State of Stress in the Earth's Crust* (W. Judd, Ed.) pp. 653–666, Elsevier, N.Y. (1965).
2. LANG T. A. Rock Mechanics Considerations in Design and Construction, *Proceedings of the Sixth Symposium on Rock Mechanics*, University of Missouri, Rolla, pp. 561–605 (1964).
3. MÜLLER L. Application of Rock Mechanics in the Design of Rock Slopes, in *State of Stress in the Earth's Crust* (W. Judd, Ed.) pp. 575–606, Elsevier, N.Y. (1965).
4. OBERL L. and DUVALL W. I. *Rock Mechanics and the Design of Underground Openings*, Wiley, N.Y. (1967).
5. SERAFIM J. L. Rock Mechanics Considerations in the Design of Concrete Dams, in *State of Stress in the Earth's Crust* (W. Judd, Ed.) pp. 575–606, Elsevier, N.Y. (1965).
6. TALOBRE J. A. The Problem of Open Pit Mine Stability, in *State of Stress in the Earth's Crust* (W. Judd, Ed.) pp. 603–610, Elsevier, N.Y. (1965).
7. ANDERSON E. M. *The Dynamics of Faulting and Dyke Formation with Application to Great Britain*, Oliver & Boyd, London (1942).
8. HUBBERT M. K. Mechanical basis for certain familiar geologic structures. *Bull. geol. Soc. Am.* **62**, 355–372 (1951).
9. BORG I. and HANDIN J. Experimental deformation of crystalline rocks. *Tectonophysics* **3**, 249–368 (1966).
10. GRIGGS D. and HANDIN J. Observations on fracture and a hypothesis of earthquakes. *Mem. geol. Soc. Am.* **79**, 347–364 (1960).
11. HANDIN J. and HAGER R. V. Jr Experimental deformation of sedimentary rock under confining pressure: Tests at room temperature on dry samples. *Bull. Am. Ass. Petrol. Geol.* **41**, 1–50 (1957).
12. ROWE P. W. Stress-dilatancy, earth pressures and slopes. *J. Soil Mech. Edns Div. Am. Soc. civ. Engrs* **SM3**, 37–61 (1963).
13. INGLIS C. E. Stresses in a plate due to the presence of cracks and sharp corners. *Trans. Instn nav. Archit.* **55**, 219–241 (1913).
14. GRIFFITH A. A. The phenomena of rupture and flow in solids. *Phil. Trans. R. Soc. A* **221**, 163–198 (1921).

15. GRIFFITH A. A. Theory of Rupture, *Proceedings of the First International Congress of Applied Mechanics*, Delft, pp. 55–63 (1924).
16. JAEGER J. C. and COOK N. G. W. *Fundamentals of Rock Mechanics*, Methuen, London (1969).
17. BRACE W. F. and BOMBOLAKIS E. G. A note on brittle crack growth in compression. *J. geophys. Res.* **68**, 3790–3813 (1963).
18. HOEK E. *Rock Fracture under Static Stress Conditions*, National Mechanical Engineering Research Institute, CSIR, Pretoria, Report MEG 383 (1965).
19. HOEK E. and BIENIAWSKI Z. T. Brittle fracture propagation in rock under compression. *Int. J. Fracture Mech.* **1**, 137–155 (1965).
20. JOHNSON A. M. *Physical Processes in Geology*, Freeman & Cooper, San Francisco (1970).
21. BALLA A. A. New solution of the stress conditions in triaxial compression. *Acta tech. hung.* **28**, 349–387 (1960).
22. CONWAY J. C. *An Investigation of the Stress Distribution in a Circular Cylinder under Static Compressive Load for varying Boundary Conditions*, M.S. Thesis, Pennsylvania State University (1963).
23. D'APPOLONIA E. and NEWMARK N. M. A Method for the Solution of the Restrained Cylinder under Compression, *Proceedings of the First U.S. Congress of Applied Mechanics*, pp. 217–226 (1951).
24. FILON N. G. On the elastic equilibrium of circular cylinders under certain practical systems of load. *Phil. Trans. R. Soc. A198*, 147–233 (1902).
25. PENG S. D. *Failure and Fracture of Chelmsford Granite*, Ph.D. Thesis, Stanford University (1970).
26. PENG S. D. Stresses within elastic circular cylinders loaded uniaxially and triaxially. To be published.
27. PICKETT G. Application of the Fourier method to the solution of certain boundary problems in the theory of elasticity. *Trans. Am. Soc. mech. Engrs* **66**, A176–A182 (1944).
28. TETELMAN A. S. and McEVILY A. J. JR *Fracture of Structural Materials*, Wiley, N.Y. (1967).
29. BIENIAWSKI Z. T. Mechanism of brittle fracture of rock. *Int. J. Rock Mech. Min. Sci.* **4**, 393–430 (1967).
30. BRACE W. F. Brittle Fracture of Rock, in *State of Stress in the Earth's Crust* (W. Judd, Ed.), pp. 111–174, Elsevier, N.Y. (1965).
31. BATEMAN P. C. *Geology and Tungsten Mineralization of the Bishop District, California*, U.S. Geological Survey Prof. Paper 470, p. 48 (1965).
32. JAHNS R. H. Personal communication (1970).
33. BELL J. F. The investigation of the cleavage of granite. *Econ. Geol.* **31**, 272–277 (1936).
34. DALE T. N. The commercial granites of New England. *Bull. U.S. geol. Surv.* **738**, 23–103 (1923).
35. OSBORNE F. F. Rift, grain and hardway in some Pre-Cambrian granites, Quebec. *Econ. Geol.* **30**, 540–551 (1935).
36. BRACE W. F. Dependence of fracture strength of rocks on grain size. *Bull. Miner. Inds. Exp. Stn Penn. St. Univ.* **76**, 99–103 (1961).
37. WESTERGAARD H. M. Bearing pressures and cracks. *Trans. Am. Soc. Mech. Engrs, J. appl. Mech.* **A49**–A53 (1939).
38. SNEDDON I. N. The distribution of stress in the neighbourhood of a crack in an elastic solid. *Proc. R. Soc. A187*, 229–260 (1946).
39. IRWIN G. R. Fracture, in *Handbuch der Physik* Vol. 4, Springer, Berlin (1958).
40. SRAWLEY J. E. and BROWN W. F. *Plane Strain Crack Toughness Testing of High Strength Metallic Materials*, ASTM, STP 440 (1966).
41. JAEGER J. C. Brittle Fracture of Rock, *Proceedings of the Eighth Symposium of Rock Mechanics*, University of Minnesota, Vol. 3, p. 57 (1967).
42. HARDY H. R. JR *Standardized Procedures for the Determination of Physical Properties of Mine Rock under Short Term Uniaxial Compression*, Mines Branch, Department of Mines and Technical Surveys, Ottawa, Report NGRL-242 (1959).
43. MCCINTOCK F. A. and WALSH J. B. Friction on Griffith Cracks under Pressure, *Proceedings of the Fourth U.S. National Congress of Applied Mechanics*, pp. 1015–1021 (1962).
44. TIMOSHENKO S. and YOUNG D. H. *Strength of Materials*, Van Nostrand, N.J. (1958).
45. TIMOSHENKO S. and GERE J. M. *Theory of Elastic Stability*, McGraw-Hill, N.Y. (1964).